

LJMU Research Online

Rehemtulla, N, Jacobson-Galán, WV, Singh, A, Miller, AA, Kilpatrick, CD, Hinds, K-R, Liu 刘, C 畅, Schulze, S, Sollerman, J, Jegou du Laz, T, Ahumada, T, Auchettl, K, Brennan, SJ, Coughlin, MW, Fremling, C, Gangopadhyay, A, Perley, DA, Prusinski, NZ, Purdum, J, Qin, Y-J, Romagnoli, S, Shi, J, Wise, JL, Chen, TX, Groom, SL, Jones, DO, Kasliwal, MM, Smith, R, Sravan, N and Kulkarni, SR

The BTSbot-nearby Discovery of SN 2024jlf: Rapid, Autonomous Follow-up Probes Interaction in an 18.5 Mpc Type IIP Supernova

<https://researchonline.ljmu.ac.uk/id/eprint/26506/>

Article

Citation (please note it is advisable to refer to the publisher's version if you intend to cite from this work)

Rehemtulla, N, Jacobson-Galán, WV, Singh, A, Miller, AA, Kilpatrick, CD, Hinds, K-R, Liu 刘, C 畅, Schulze, S, Sollerman, J, Jegou du Laz, T, Ahumada, T, Auchettl, K, Brennan, SJ, Coughlin, MW, Fremling, C, Gangopadhyay, A, Perley, DA, Prusinski, NZ, Purdum, J, Qin, Y-J.

LJMU has developed **LJMU Research Online** for users to access the research output of the University more effectively. Copyright © and Moral Rights for the papers on this site are retained by the individual authors and/or other copyright owners. Users may download and/or print one copy of any article(s) in LJMU Research Online to facilitate their private study or for non-commercial research. You may not engage in further distribution of the material or use it for any profit-making activities or any commercial gain.

The version presented here may differ from the published version or from the version of the record. Please see the repository URL above for details on accessing the published version and note that access may require a subscription.

For more information please contact researchonline@ljmu.ac.uk



The BTSbot-nearby Discovery of SN 2024jlf: Rapid, Autonomous Follow-up Probes Interaction in an 18.5 Mpc Type IIP Supernova

Nabeel Rehemtulla^{1,2,3} , W. V. Jacobson-Galán^{4,16} , Avinash Singh⁵ , Adam A. Miller^{1,2,3} , Charles D. Kilpatrick² , K-Ryan Hinds⁶ , Chang Liu (刘畅)^{1,2} , Steve Schulze² , Jesper Sollerman⁵ , Theophile Jegou du Laz⁷ , Tomás Ahumada⁷ , Katie Auchetti^{8,9} , S. J. Brennan⁵ , Michael W. Coughlin¹⁰ , Christoffer Fremling^{7,11} , Anjasha Gangopadhyay⁵ , Daniel A. Perley⁶ , Nikolaus Z. Prusinski¹² , Josiah Purdum¹¹ , Yu-Jing Qin⁷ , Sara Romagnoli⁹ , Jennifer Shi⁹ , Jacob L. Wise⁶ , Tracy X. Chen¹³ , Steven L. Groom¹³ , David O. Jones¹⁴ , Mansi M. Kasliwal⁷ , Roger Smith¹¹ , Niharika Sravan¹⁵, and Shrinivas R. Kulkarni⁷

¹ Department of Physics and Astronomy, Northwestern University, 2145 Sheridan Road, Evanston, IL 60208, USA; nabeelr@u.northwestern.edu

² Center for Interdisciplinary Exploration and Research in Astrophysics (CIERA), 1800 Sherman Ave., Evanston, IL 60201, USA

³ NSF-Simons AI Institute for the Sky (SkAI), 172 E. Chestnut St., Chicago, IL 60611, USA

⁴ Department of Astronomy and Astrophysics, California Institute of Technology, Pasadena, CA 91125, USA

⁵ Department of Astronomy, The Oskar Klein Center, Stockholm University, AlbaNova, SE-10691 Stockholm, Sweden

⁶ Astrophysics Research Institute, Liverpool John Moores University, IC 2, Liverpool Science Park, 146 Brownlow Hill, Liverpool L3 5RF, UK

⁷ Division of Physics, Mathematics, and Astronomy, California Institute of Technology, Pasadena, CA 91125, USA

⁸ Department of Astronomy and Astrophysics, University of California, Santa Cruz, Santa Cruz, CA 95064, USA

⁹ OzGrav, School of Physics, The University of Melbourne, VIC 3010, Australia

¹⁰ School of Physics and Astronomy, University of Minnesota, Minneapolis, MN 55455, USA

¹¹ Caltech Optical Observatories, California Institute of Technology, Pasadena, CA 91125, USA

¹² Cahill Center for Astronomy and Astrophysics, California Institute of Technology, MC 249-17, Pasadena, CA 91125, USA

¹³ IPAC, California Institute of Technology, 1200 E. California Blvd., Pasadena, CA 91125, USA

¹⁴ Institute for Astronomy, University of Hawai'i, 640 N. A'ohoku Pl., Hilo, HI 96720, USA

¹⁵ Department of Physics, Drexel University, Philadelphia, PA 19104, USA

Received 2025 February 3; revised 2025 April 15; accepted 2025 April 20; published 2025 May 29

Abstract

We present observations of the Type IIP supernova (SN) SN 2024jlf, including spectroscopy beginning just 0.7 days (~ 17 hr) after first light. Rapid follow-up was enabled by the new BTSbot-nearby program, which involves autonomously triggering target-of-opportunity requests for new transients in Zwicky Transient Facility data that are coincident with nearby ($D < 60$ Mpc) galaxies and identified by the BTSbot machine learning model. Early photometry and nondetections shortly prior to first light show that SN 2024jlf initially brightened by > 4 mag day $^{-1}$, quicker than $\sim 90\%$ of Type II SNe. Early spectra reveal weak flash ionization features: narrow, short-lived ($1.3 < \tau[\text{days}] < 1.8$) emission lines of H α , He II, and C IV. Assuming a wind velocity of $v_w = 50$ km s $^{-1}$, these properties indicate that the red supergiant progenitor exhibited enhanced mass loss in the last year before explosion. We constrain the mass-loss rate to $10^{-4} < \dot{M} [M_\odot \text{ yr}^{-1}] < 10^{-3}$ by matching observations to model grids from two independent radiative hydrodynamics codes. BTSbot-nearby automation minimizes spectroscopic follow-up latency, enabling the observation of ephemeral early-time phenomena exhibited by transients.

Unified Astronomy Thesaurus concepts: Core-collapse supernovae (304); Type II supernovae (1731); Spectroscopy (1558); Sky surveys (1464); Time domain astronomy (2109); Transient sources (1851)

Materials only available in the online version of record: machine-readable tables

1. Introduction

Following shock breakout in core-collapse supernovae (CCSNe), the shock front propagates outward and photoionizes the surrounding medium. Circumstellar material (CSM) in the vicinity will also be photoionized as the shock progresses, and, should the CSM be at high enough density, the subsequent recombination will produce “flash,” or “IIn-like,” features (A. Gal-Yam et al. 2014): narrow ($v \lesssim 100$ km s $^{-1}$), short-lived (\sim days) emission lines of highly ionized species (e.g., He II, C III/IV, N III/IV/V, O VI). CSM with lower density (i.e., that arising from a progenitor with

mass-loss rate $\dot{M} \lesssim 10^{-5} M_\odot \text{ yr}^{-1}$) will recombine within hours after shock breakout and not provide significant forward shock luminosity.

The properties of an event’s flash features are directly linked to physical properties, namely, the CSM extent and mass and the chemical composition of the progenitor star’s surface prior to the SN. Critically, properties of flash features also imply that the progenitor star underwent an episode of enhanced mass loss shortly before the SN: the high-ionization features imply that the CSM is dense, and the short duration suggests that the CSM is close-in to the progenitor star. Comparison to sophisticated radiative hydrodynamic models (e.g., those from L. Dessart et al. 2017; I. Boian & J. H. Groh 2019; L. Dessart & W. V. Jacobson-Galán 2023; T. J. Moriya et al. 2023) enables the inference of these parameters (e.g., I. Shivvers et al. 2015; I. Boian & J. H. Groh 2020; J. Zhang et al. 2020; L. Tartaglia et al. 2021; W. V. Jacobson-Galán et al. 2022; G. Terreran et al. 2022; J. E. Andrews et al. 2024). Progenitor

¹⁶ NASA Hubble Fellow.



mass-loss rates in the years before explosion have been inferred to upward of $10^{-2} M_{\odot} \text{ yr}^{-1}$ for some “flashing” SNe (e.g., SN 2023ixf, E. Berger et al. 2023; K. A. Bostroem et al. 2023; D. Hiramatsu et al. 2023; W. V. Jacobson-Galán et al. 2023; R. S. Teja et al. 2023; A. Singh et al. 2024; E. A. Zimmerman et al. 2024; SN 2024ggi, W. V. Jacobson-Galán et al. 2024a; M. Shrestha et al. 2024). These \dot{M} in the years before explosion are orders of magnitude higher than that of Milky Way red supergiants (RSGs; $\dot{M} \approx 10^{-6} M_{\odot} \text{ yr}^{-1}$; E. R. Beasor et al. 2020) and that inferred for Type IIP SNe (SNe IIP) without flash features (e.g., SN 2017eaw; C. D. Kilpatrick & R. J. Foley 2018; T. Szalai et al. 2019).

Flash features have historically been difficult to study, in large part due to their ephemeral nature. V. S. Niemela et al. (1985) published the first SN spectra exhibiting flash features, and O. Yaron et al. (2017) published a remarkable data set on SN 2013fs, now a prototypical example of flashing SNe II. The search for these features (“flash spectroscopy”) has produced samples of SNe II with spectra shortly after first light, including dozens of events exhibiting flash features (D. Khazov et al. 2016; R. J. Bruch et al. 2021, 2023; W. V. Jacobson-Galán et al. 2024b). Short-lived narrow emission features have also been seen in SNe from stripped stars (e.g., A. Gangopadhyay et al. 2020, 2022; D. A. Perley et al. 2022; K. W. Davis et al. 2023; S. Schulze et al. 2024), but we discuss only SNe II here.

R. J. Bruch et al. (2023, hereafter B23; preceded by R. J. Bruch et al. 2021 and accompanied by I. Irani et al. 2024) search for narrow He II $\lambda 4686$ emission in SNe II, which they use to define an SN as flashing. They unambiguously identify such emission in at least 30% of events in their sample, while more than half have moderately confident detections. They also find no significant difference in the optical light-curve properties (rise time, peak magnitude, color at peak) of flashing and nonflashing events, while I. Irani et al. (2024) find that flashers have larger initial blackbody radii and luminosities. Crucially, I. Irani et al. (2024) find that many SNe II do not fit shock cooling models well in the early time but do later on in their evolution, underscoring the importance of well-sampled early optical and UV light curves. B23 quantify the duration of flash features (τ) as the duration for which narrow He II $\lambda 4686$ emission is visible. The events in their sample typically have $\tau \gtrsim 5$ days, and they find tentative evidence for an additional population of rare events with long-lived flash features ($\tau > 10$ days).

W. V. Jacobson-Galán et al. (2024b, hereafter JG24) focus on features matching slightly different criteria that they call “IIn-like”: symmetric, narrow, short-lived features with Lorentzian wings. The Lorentzian wings are caused by electron scattering before photons escape from the CSM.¹⁷ Which species are seen exhibiting IIn-like features and their relative strengths determines which of three classes JG24 classifies an SN II as. They find that each of these classes exhibits a different distribution of IIn-like feature duration (t_{IIn}) and that there are clear differences in light-curve properties (peak optical and UV magnitude and pseudobolometric luminosity) between flashing and nonflashing events.

Still, there remain large uncertainties in the results of these sample studies, primarily due to the relatively small sample sizes and the lack of systematic follow-up observations.

Addressing these challenges necessitates observational campaigns that start sooner after explosion and continue with high-cadence, high signal-to-noise ratio spectroscopy at least until the narrow features have subsided, an important transition for distinguishing flashing SNe II from SNe IIn.

The favored facilities for finding SNe shortly after explosion are wide-field time-domain surveys like the Asteroid Terrestrial Last-Alert System (ATLAS; J. L. Tonry 2011; J. L. Tonry et al. 2018; K. W. Smith et al. 2020), Distance Less Than 40 (DLT40; L. Tartaglia et al. 2018), the Young Supernova Experiment (YSE; D. O. Jones et al. 2021) on the Pan-STARRS telescopes (Panoramic Survey Telescope and Rapid Response System; N. Kaiser et al. 2002), and the Zwicky Transient Facility (ZTF; E. C. Bellm et al. 2019b, 2019a; M. J. Graham et al. 2019; F. J. Masci et al. 2019; R. Dekany et al. 2020). The early stages of the established real-time workflows in these surveys, e.g., data reduction, alert generation, and real/bogus classification (J. S. Bloom et al. 2012; H. Brink et al. 2013), are typically fully automated. SN discovery, however, relies almost entirely on visual inspection of SN candidates (or “scanning”). Because of this, humans are among the greatest sources of latency between a survey collecting data and follow-up spectroscopy being obtained for a new SN in those data.

Latency in transient workflows can be minimized by automating the process of transient identification and follow-up. Doing so introduces two key challenges: (i) spectroscopic resources are extremely valuable, so identifications following filtering must be made with very low false-positive (FP) rates, and (ii) truly minimizing latency requires making identifications with minimal data, i.e., often only two detections over one to two nights. Here we focus on the classes of relatively common optical transients (predominantly SNe) and put aside more exotic classes like gamma-ray bursts and electromagnetic counterparts to gravitational-wave events. Although the challenges are broadly similar, the multiwavelength and multimessenger nature of these events makes the workflows quite different (e.g., V. D’Elia et al. 2009). Many tools exist for automatically identifying and characterizing SN candidates, but few satisfy both criteria, making them unfit for autonomous low-latency SN follow-up. Photometric transient classification tools (e.g., K. Boone 2019; D. Muthukrishna et al. 2019; V. A. Villar et al. 2019, 2020; A. Gagliano et al. 2023) often require days to weeks of data to perform well. Many other tools focus on rare types of transients and thus typically compromise purity to maximize the number of recovered events (e.g., S. Gomez et al. 2020, 2023; R. Stein et al. 2024). Tools that perform high-level classification of events (e.g., transient vs. other) on real-time alert streams, however, are better suited for this task (e.g., R. Carrasco-Davis et al. 2021; D. A. Duev & S. J. van der Walt 2021; N. Rehemtulla et al. 2024b).

One such tool is BTSbot (N. Rehemtulla et al. 2024b), a machine learning model for autonomously identifying bright ($m_{\text{peak}} \leq 18.5$ mag) extragalactic transients in the ZTF data stream. BTSbot was designed to select targets for the ZTF Bright Transient Survey (BTS; C. Fremling et al. 2020; D. A. Perley et al. 2020; N. Rehemtulla et al. 2024b), which endeavors to spectroscopically classify all such sources. BTSbot was deployed into ZTF and BTS operations in 2023 October with the ability to autonomously trigger follow-up to the SED Machine (SEDM; N. Blagorodnova et al. 2018;

¹⁷ Hence the name IIn-like, as this is similar to the process that forms the narrow features present in SNe IIn.

Y. L. Kim et al. 2022). Since then, it has sent >1200 automated spectroscopic follow-up requests, many of which are on transients it identified before human scanners in BTS. Close monitoring of triggers in the first 8 months of operations revealed that $\sim 96\%$ of BTSbot identifications were of genuine extragalactic transients, matching expected performance (N. Rehemtulla et al. 2024b).

The discovery and follow-up of SN 2024jlf demonstrated the efficacy of automating rapid-response follow-up of quickly evolving transients. This was done with a new program repurposing the BTSbot model: BTSbot-nearby. SN 2024jlf was an SN IIP, the core-collapse explosion of an RSG star (see, e.g., M. Hamuy 2003; O. Pejcha & J. L. Prieto 2015, for reviews). After reaching peak luminosity, these events exhibit a characteristic prolonged light-curve plateau phase (encoded by the “P” in “SN IIP”) where the SN remains roughly constant in luminosity for ~ 100 days (N. N. Chugai 1991). Spectroscopic observations during this phase reveal broad hydrogen Balmer P Cygni features.

Early spectroscopic observations of SN 2024jlf revealed flash features in He II, C IV, and H α . We match observations of SN 2024jlf to models produced with sophisticated radiation hydrodynamic simulations in order to infer properties of the progenitor star and CSM. We also discuss discrepancies in values inferred from models produced with different simulation codes.

Throughout this study we assume a flat Λ CDM cosmology with $H_0 = 70 \text{ km s}^{-1} \text{ Mpc}^{-1}$ and $\Omega_M = 0.3$. All times here are in UTC unless otherwise noted, and all magnitudes are in the AB system unless otherwise noted.

2. BTSbot-nearby

We present BTSbot-nearby, a new autonomous, rapid follow-up program for nearby ($D < 60 \text{ Mpc}$) infant SNe in ZTF data. This program involves repurposing the BTSbot model and introducing new filtering to identify nearby infant SNe with a very low FP rate.

The BTSbot-nearby alert filter¹⁸ is based on that used by BTS and BTSbot (see D. A. Perley et al. 2020) and the ZTF Census of the Local Universe experiment (CLU; K. De et al. 2020).

We make some minor adjustments to criteria in these filters. The real/bogus score threshold using braai (D. A. Duev et al. 2019), ZTF’s deep learning model for filtering of nonastrophysical alerts, is increased from 0.3 (in the BTS alert filter) to 0.7. This adjustment is made to more consistently reject bogus alerts that frequently occur atop very bright galactic nuclei. Such backgrounds are common for nearby transients, and alerts from these areas tend to be misclassified by braai. Based on Figure 9 of D. A. Duev et al. (2019), this should reduce the real/bogus FP rate from $\sim 3.6\%$ to $\sim 1.6\%$. We also make the rejection of candidates based on cross-matches to the Minor Planet Center (MPC) catalog more strict; a source with any alert within $2''$ of an MPC object will be rejected.

The primary addition is filtering following host galaxy association. Alerts only pass the BTSbot-nearby filter if they are coincident with a NASA Extragalactic Database Local Volume Sample (NED-LVS; D. O. Cook et al. 2023;

D. Cook et al. 2025) galaxy that has distance $D < 60 \text{ Mpc}$. An alert is considered coincident with a galaxy if its projected physical offset is $\leq 15 \text{ kpc}$, capped at a maximum angular offset of $2'$. The angular offset limit is imposed because the size of the selection region for very nearby galaxies ($D \lesssim 1 \text{ Mpc}$) is otherwise extremely large and prone to selecting sources unrelated to the nearby galaxy. The 60 Mpc limit is motivated by the ZTF sensitivity: a 20.5 mag source at 60 Mpc corresponds to having an absolute magnitude of roughly -13.5 mag , sufficient to capture SNe very early. An offset limit of 15 kpc selects the vast majority of CCSNe and SNe Ia (C. Fremling et al. 2020; S. Schulze et al. 2021) while limiting contamination from sources projected nearby but unrelated to a galaxy.

Once a source is associated with a galaxy, the galaxy’s distance can be used to estimate the source’s absolute magnitude. BTSbot-nearby requires that the source have absolute magnitude in any ZTF filter of $M < -11 \text{ mag}$ to reject variable stars and classical novae that are visible to ZTF in the most nearby galaxies (e.g., M31 and M33; M. Capaccioli et al. 1989). The source must also have at least one alert with a BTSbot score greater than 0.5. This criterion is crucial for rejecting remaining contamination like non-SN stellar activity in very nearby galaxies, active galactic nuclei (AGN) and cataclysmic variables projected over nearby galaxies, and more. The target must also not be coincident with a source on the Transient Name Server (TNS)¹⁹ that was reported more than 36 hr before the time of filtering. Next, we select only sources with nondetections within 3.5 days of the latest alert to ensure that those transients that are selected are very young. The final criterion considers the status of the source on ZTF’s first-party marshal Fritz²⁰ (a SkyPortal instance; S. J. van der Walt et al. 2019; M. W. Coughlin et al. 2023); a trigger is prevented if there is (i) an existing spectroscopic follow-up request, (ii) a classification assigned, or (iii) a spectrum already present. The criteria involving the status of the source on Fritz are described in detail in Appendix B of N. Rehemtulla et al. (2024b). Once all criteria are met, follow-up requests can be triggered with configurable parameters.

BTSbot-nearby filtering runs on ZTF’s first-party alert broker, Kowalski (D. A. Duev et al. 2019), and marshal, Fritz, which support triggering automated follow-up to numerous other facilities.

2.1. Quality of BTSbot-nearby Filtering Relative to Human Scanning

We characterize the quality of the BTSbot-nearby filtering by assessing the completeness (or “recall”) and purity (or “precision”) of triggers and comparing the latency of automated follow-up with that of traditional, human-triggered follow-up. We pass ZTF public and partnership alerts from the main surveys between 2023 October 1 and 2025 April 1²¹ through the BTSbot-nearby filters and log which sources satisfy them and whether they are true positives (TPs) or FPs. False negatives (FNs) are identified by cross-matching with sources cataloged in BTS or CLU during the same time frame.

¹⁹ <https://www.wis-tns.org>

²⁰ <https://github.com/fritz-marshall/fritz>

²¹ The dates are determined by when the latest version of BTSbot was deployed into production and when this analysis was conducted.

¹⁸ BTSbot-nearby was initially introduced in N. Rehemtulla et al. (2024a). Here we describe the most up-to-date version of the filtering.

Statistics are calculated identically to how they were by N. Rehemtulla et al. (2024b). A total of 77 sources satisfy the BTSbot-nearby filtering in this time frame; $\sim 90\%$ of these are genuine nearby transients, identified via cross-match with BTS/CLU catalogs and visual inspection. The FPs are strongly dominated by distant transients that are erroneously cross-matched to nearby galaxies but also include small numbers of AGN and cataclysmic variable stars. The count of FNs is definition dependent. In most cases, BTS/CLU transients were not selected by BTSbot-nearby filtering because their host galaxies do not appear in the NED catalog used. In some cases, the host galaxies had entries in NED but lacked either a spectroscopic redshift or a redshift-independent distance measurement. Transients that are very highly offset from their host represent a very small but astrophysically important population of FNs. These results suggest that the host galaxy association mechanism used by BTSbot-nearby can still be improved.

To illustrate the minimization of follow-up latency with BTSbot-nearby, we define metrics to compare with the established filtering and follow-up in ZTF. We measure the “spectroscopic follow-up latency” (Δt_{spec}) as the time between when a source first passes the alert filter, i.e., when it is then available for humans to scan or BTSbot to identify, and when the first spectrum of the source is taken. This metric is favorable because it is not sensitive to the ZTF observing strategy or to variations in processing time at IPAC, while also not limiting the analysis to a subset of spectrographs used. The time of a follow-up request being submitted is not used because it is only attainable for SEDM requests. We compute this metric for $D \lesssim 60$ Mpc SNe between 2021 January 1 (around when the BTS alert filter was last improved) and 2024 October 1 (when this analysis was conducted). We also limit this analysis to transients for which ZTF is listed as the discovery data source on TNS to exclude cases where follow-up may have been motivated by external data, for example, from another survey, which would bias the latency distribution.

Figure 1 shows the distribution of spectroscopic follow-up latencies for nearby SNe, highlighting those involving BTSbot and that which was demonstrated by BTSbot-nearby for SN 2024jlf. Latencies for SNe with human-triggered follow-up clearly cluster around $\Delta t_{\text{spec}} = 1$ day. This matches expectations for this time period because visual inspection and triggering of high-priority follow-up typically only occur the morning after observations. When this is the case and the follow-up instrument is colocated with the survey (e.g., ZTF and SEDM), follow-up tends to occur ~ 24 hr after discovery. This amount of latency or more is reflected in the results of numerous infant SN studies, including those that deal with UV follow-up; see, e.g., Figure 2 of I. Irani et al. (2024).

This is not always the case, however. Scanners in Europe are able to easily scan in near real-time because the Palomar night coincides with morning and afternoon in Europe. This has resulted in countless instances of early follow-up triggered by European scanners yielding valuable results (e.g., J. Sollerman et al. 2021; S. Yang et al. 2021). In fact, much of the follow-up effort supporting R. J. Bruch et al. (2021) and B23 was enabled by scanners in Europe. Because the sample used here is bounded by 2021 January 1, it does not contain any SNe in B23, but the latency statistics are representative for human scanning between 2021 January and 2024 October.

Comparing the BTSbot latencies with that of human scanners in Figure 1 shows that most follow-up involving

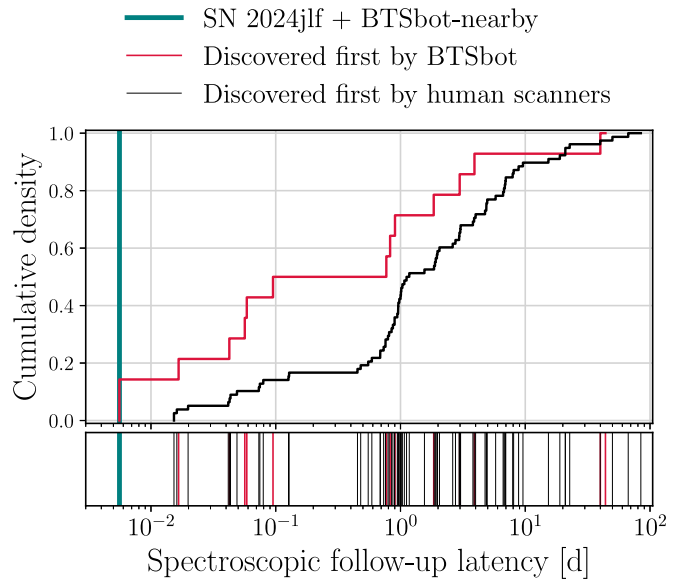


Figure 1. Comparison of spectroscopic follow-up latency (Δt_{spec}) distributions for automated (red, teal) and manual (black) follow-up of nearby ($D < 60$ Mpc) SNe discovered in ZTF data. Δt_{spec} is the time between an SN passing a ZTF alert filter and the first spectrum being taken. Relying on human-triggered follow-up often incurs $\Delta t_{\text{spec}} \gtrsim 1$ day of latency, whereas automated follow-up can expedite Δt_{spec} by an order of magnitude. BTSbot-nearby demonstrated $\Delta t_{\text{spec}} \approx 7$ minutes for SN 2024jlf.

BTSbot is much quicker: $\Delta t_{\text{spec}} \ll 1$ day. The event with the single lowest latency in this sample is SN 2024jlf: $\Delta t_{\text{spec}} \approx 7$ minutes. Automating transient identification and the triggering of rapid-response follow-up mitigates costly latency. With extremely small latencies, observations can probe the mostly unexplored earliest phases, i.e., hours after first light, of extragalactic transients.

3. Observations of SN 2024jlf

3.1. Discovery and Classification

SN 2024jlf was first reported to TNS by K. Hinds et al. (2024) at 10:29:59 on 2024 May 28 (modified Julian date; MJD 60458.44) using data from ZTF (internal name ZTF24aaozxhx), which measured its brightness to $g_{\text{ZTF}} = 15.88 \pm 0.04$ mag. It has been localized in NGC 5690 to $\alpha_{\text{J2000}} = 14^{\text{h}}37^{\text{m}}42^{\text{s}}.32$, $\delta_{\text{J2000}} = +02^{\circ}17'04''.12$. About 3 hr later, G. Hosseinzadeh et al. (2024) and the Global SN Project (D. A. Howell & Global Supernova Project 2017) classified SN 2024jlf as a young SN II and noted that it displayed weak flash features.

Before either TNS report, BTSbot identified ZTF24aaozxhx as a genuine bright ($m_{\text{peak}} < 18.5$ mag) transient, saved it to an internal ZTF transient catalog, and triggered a high-priority follow-up request for photometry (*ugri*) and spectroscopy to SEDM at 07:53:40 (MJD 60458.33).²² SEDM began observing ZTF24aaozxhx just ~ 7 minutes later at 08:00:51; this observation occurred only $+0.7$ days after first light (see Section 3.3.1 for details). Logs of Fritz activity, where ZTF partners scan new transient candidates, suggest that no astronomer in ZTF had viewed ZTF24aaozxhx before the spectroscopic observation had concluded. Following this discovery, we collected multiwavelength, high-cadence

²² In the future, BTSbot-nearby discoveries will automatically be reported to TNS to facilitate community follow-up of these important targets.

Table 1
Basic Properties of SN 2024jlf

Property	Value
Distance modulus μ (mag)	31.33 ± 0.43
Luminosity distance D_L (Mpc)	18.45 ± 3.66
z_{SDSS}	0.00592 ± 0.00002
EW_{NaID} (Å)	0.815 ± 0.033
$A_{V,\text{host}}$ (mag)	0.636 ± 0.122
$A_{V,\text{MW}}$ (mag)	0.120
MJD of first light t_h	60457.62 ± 0.054
$M_{u,\text{peak}}$ (mag)	$-17.10^{+0.10}_{-0.10}$
$M_{g,\text{peak}}$ (mag)	$-16.97^{+0.072}_{-0.071}$
$M_{r,\text{peak}}$ (mag)	$-16.78^{+0.064}_{-0.064}$
$M_{i,\text{peak}}$ (mag)	$-16.58^{+0.13}_{-0.14}$
Duration of flash features τ (days)	1.3–1.8

follow-up observations with numerous facilities to probe the evolution of SN 2024jlf.

3.2. Host Galaxy—NGC 5690

SN 2024jlf occurred in NGC 5690, an edge-on spiral galaxy showing prominent dust lanes. G. de Vaucouleurs et al. (1991) classify NGC 5690 as a possible Sc galaxy, with some uncertainty due to the edge-on orientation. The distance modulus to NGC 5690 is measured to be $\mu = 31.33 \pm 0.43$ mag by J. G. Sorce et al. (2014) using the Tully–Fisher relation (R. B. Tully & J. R. Fisher 1977); this corresponds to a luminosity distance of $D_L = 18.45 \pm 3.7$ Mpc. A Sloan Digital Sky Survey (SDSS; D. G. York et al. 2000) spectrum of the galaxy’s nucleus yields $z_{\text{SDSS}} = 0.00592 \pm 0.00002$ (F. D. Albareti et al. 2017). We adopt these values as the distance modulus, distance, and redshift to SN 2024jlf, and they are summarized in Table 1.

NGC 5690 has been imaged by the InfraRed Array Camera (IRAC; G. G. Fazio et al. 2004) on the Spitzer Space Telescope (Spitzer) through multiple Spitzer programs: PID 14098 (PI O. Fox), PID 61066 (PI K. Sheth), and PID 10046 (PI D. Sanders). We stack the available $3.6 \mu\text{m}$ and $4.5 \mu\text{m}$ imagery to search for the progenitor of SN 2024jlf but are unable to detect a source at the SN location.

We use the equivalent width of the Na ID doublet as a proxy for the reddening toward the SN due to the host galaxy. This practice, although very common, has important caveats (D. Poznanski et al. 2011; M. M. Phillips et al. 2013). We directly integrate a continuum-normalized spectrum over the Na ID region (see Figure 2) to compute an equivalent width of $EW_{\text{NaID}} = 0.815 \pm 0.033$ Å. The uncertainty reported is the standard deviation of 1000 trials of recomputing the equivalent width using Monte Carlo samples of the flux and its uncertainty. Using the relation in M. D. Stritzinger et al. (2018), we compute $A_{V,\text{host}} = 0.636 \pm 0.122$ mag. Section 3.3 describes how reddening correction is applied to the photometry given this $A_{V,\text{host}}$. Figure 2 also illustrates that the velocity of the sodium gas producing the absorption is moving at 80 km s^{-1} relative to the galaxy nucleus, as measured by the SDSS spectrum.

3.3. Photometric Observations

The ZTF public and partnership surveys observed SN 2024jlf from the initial discovery to when the field moved

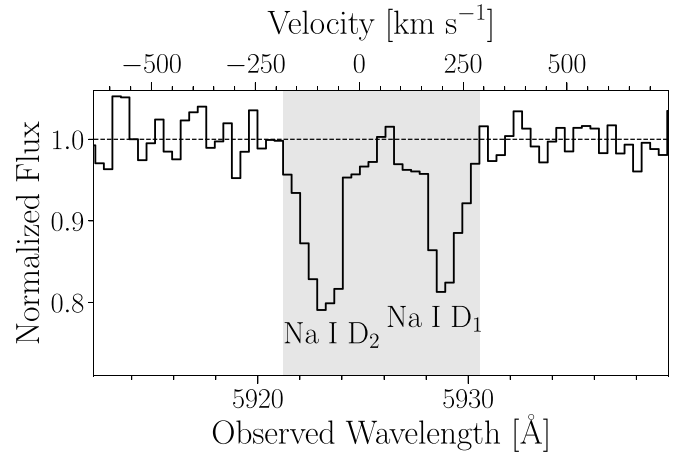


Figure 2. Na ID absorption doublet (shaded gray region) in a continuum-normalized spectrum of SN 2024jlf (solid black line). The large equivalent width, measured to be 0.815 ± 0.033 Å, suggests significant extinction by the host galaxy. The velocity axis is defined relative to the Na I D₂ line at the host redshift from SDSS. The sodium gas producing the absorption appears to move with $v = 80 \text{ km s}^{-1}$ relative to the host nucleus, where the SDSS fiber is placed.

behind the Sun. We obtain forced point-spread function (PSF) photometry from the ZTF forced-photometry service (F. J. Masci et al. 2019, 2023), which we then process to calibrated flux measurements with the pipeline presented in A. A. Miller et al. (2025, in preparation).

YSE (D. O. Jones et al. 2021) monitoring with the Pan-STARRS1 (PS1) telescope (N. Kaiser et al. 2002) produced deep nondetections shortly before the first detection by ZTF and several detections afterward. All YSE data were processed using photpipe (A. Rest et al. 2005) following methods described in D. O. Jones et al. (2021), including digital image subtraction with PS1 3π templates (K. C. Chambers et al. 2016) using HOTPANTS (A. Becker 2015). All YSE photometry and pre-explosion limits presented here are derived from forced photometry in the difference images.

We conducted optical imaging of SN 2024jlf with the SEDM Rainbow Camera (RC) on board the P60 telescope (S. B. Cenko et al. 2006) and the Sinistro imager at Sliding Spring Observatory in the Las Cumbres Observatory (LCO) 1 m telescope network (T. M. Brown et al. 2013). SEDM RC observations were reduced with the FPIPE automated subtraction pipeline (C. Fremling et al. 2016). Sinistro images were reduced using photpipe following similar methods to our YSE data. As pre-explosion images were not available in each band, we did not perform image subtraction in the LCO imaging and instead report dophot (P. L. Schechter et al. 1993) PSF photometry for all detections coincident with SN 2024jlf in the unsubtracted images. This potentially introduces a small systematic bias relative to the rest of our optical photometry, which is derived in difference imaging.

SN 2024jlf was observed in the UV (UVW1, UVW2, UVM2) and near-UV (U_S) with the Ultraviolet/Optical Telescope (UVOT; P. W. A. Roming et al. 2005) on board the Neil Gehrels Swift Observatory (Swift; N. Gehrels et al. 2004). We processed all UVOT photometry of SN 2024jlf using a Python-based wrapper²³ for photometry tools in *heasoft* v6.28 (Nasa High Energy Astrophysics Science Archive Research Center

²³ https://github.com/charliekilpatrick/Swift_host_subtraction

Table 2
Optical and UV Photometry of SN 2024jlf

t_{obs} (MJD)	Filter	m (mag)	σ_m (mag)	Telescope/Instrument
60458.25	g_{ZTF}	15.878	0.0133	P48/ZTF
60458.32	i_{ZTF}	16.239	0.0169	P48/ZTF
60458.33	r'	15.991	0.0405	P60/SEDM
60458.33	r'	15.991	0.054	P60/SEDM
60458.34	r_{ZTF}	16.055	0.0236	P48/ZTF

Note. Observed magnitudes in the ZTF, YSE, UVOT, SEDM, and Sinistro passbands. Correction for Galactic extinction has not been applied.

(This table is available in its entirety in machine-readable form in the [online article](#).)

Heasarc 2014). We optimally stacked each epoch and performed aperture photometry in each band using `uvotsource`.

All photometry is corrected for Milky Way and host extinction using the `extinction` package (K. Barbary 2017). We adopt the extinction law from E. L. Fitzpatrick (1999), $R_{V,\text{MW}} = R_{V,\text{host}} = 3.1$, and the dust map from E. F. Schlafly & D. P. Finkbeiner (2011) queried using the `dustmaps` package (G. Green 2018; G. Green et al. 2024). The dust map yields $E(B - V)_{\text{MW}} = 0.039$ mag, which corresponds to $A_{V,\text{MW}} = 0.120$ mag. The reddening from the host is applied using $A_{V,\text{host}} = 0.636 \pm 0.122$ mag, computed from the equivalent width of the Na ID doublet (see Section 3.2). Lastly, we inflate the magnitude uncertainties by 2% to account for otherwise unconsidered systematics. All photometry is reported in Table 2.

The final light curve is shown in Figure 3. The right panel shows the full light curve including a steep rise and ~ 85 -day plateau. The left panel zooms in on the early light curve and makes clear the exceptionally quick rise of SN 2024jlf. Short vertical lines across the bottom of the figure represent each epoch of spectroscopic observations. Best-fit model light curves are also shown and discussed in Sections 4.2 and 5.

We compare the observed light-curve properties with those of 459 ZTF SNe II from K.-R. Hinds et al. (2025). Figure 4 shows the g -band absolute magnitude and rise time (defined as time from 25% to 75% of maximum flux), both inferred from Gaussian process fits performed in K.-R. Hinds et al. (2025, in preparation). We find that SN 2024jlf rises quicker than $\sim 90\%$ of SNe II in the sample and peaks in the g band slightly fainter than average. This extremely rapid rise is likely a product of early-time flux excess originating from CSM interaction.

This is consistent with the findings of JG24, where it is shown that SNe II with weak/intermediate CSM interaction tend to rise quicker than those without.

3.3.1. Basic Light-curve Parameters

We fit low-order polynomials to each of the optical bands to infer their peak magnitudes. The values reported in Table 1 are the median and 1σ bounds from performing 10,000 Monte Carlo samples of the polynomial parameter uncertainties produced by the fit. Although each instrument uses slightly different filter systems, i.e., g_{ZTF} for ZTF, g_{PS1} for YSE, and g' for SEDM and Sinistro, we approximate these as the same when performing this modeling.

We also jointly fit power laws to the early gri photometry to infer the time of first light. The power laws are each in the form

$$F_{\nu}(t) = \begin{cases} a(t - t_{\text{fl}})^b & \text{if } t \geq t_{\text{fl}} \\ 0 & \text{if } t < t_{\text{fl}} \end{cases}, \quad (1)$$

where a and b can vary for each filter, but t_{fl} is fixed across all filters (A. A. Miller et al. 2020). Figure 5 shows the power laws that result from this procedure. The very late YSE nondetection and the rapid follow-up allow us to constrain the time of first light to $t_{\text{fl}} = 60457.62 \pm 0.054$ MJD. We adopt this value throughout this study.

3.4. Spectroscopic Observations

We conducted a thorough spectroscopic follow-up campaign to monitor the evolution of SN 2024jlf out to +94.6 days after t_{fl} . Spectroscopic follow-up was conducted with numerous facilities: SEDM (N. Blagorodnova et al. 2018; Y. L. Kim et al. 2022) on the P60 telescope (S. B. Cenko et al. 2006), the Spectrograph for the Rapid Acquisition of Transients (SPRAT; A. S. Piascik et al. 2014) on the robotic 2 m Liverpool Telescope (LT; I. A. Steele et al. 2004), the Alhambra Faint Object Spectrograph and Camera (ALFOSC)²⁴ on the 2.56 m Nordic Optical Telescope (NOT), Binospec (D. Fabricant et al. 2019) on the 6.5 m MMT telescope, the Low Resolution Imaging Spectrometer (LRIS; J. B. Oke et al. 1995) on the W. M. Keck Observatory's Keck I 10 m telescope, the Keck Cosmic Web Imager (KCWI; C. Martin et al. 2010; P. Morrissey et al. 2018) on the Keck II 10 m telescope, and the Wide-Field Spectrograph (WiFeS; M. Dopita et al. 2007, 2010) on the Australian National University 2.3 m (ANU) Advanced Technology Telescope (ATT) at Siding Spring Observatory. We also include the FLOYDS-N spectrum uploaded to TNS by G. Hosseinzadeh et al. (2024).

The SEDM observations are reduced by the custom `pySEDM` package (M. Rigault et al. 2019). Spectra from other facilities are reduced with standard procedures (see T. Mattheson et al. 2000). Reduction of MMT/Binospec and Keck/LRIS spectra uses `pypeit` (J. X. Prochaska et al. 2020), LT/SPRAT reduction uses the custom FRODOSpec pipeline (R. M. Barnsley et al. 2012), NOT/ALFOSC reduction uses a custom `pypeit`-based script,²⁵ Keck/KCWI reduction uses the official data reduction pipeline,²⁶ and ANU/WiFeS reduction uses `PyWiFeS` (see M. J. Childress et al. 2014; A. Carr et al. 2024).²⁷ Our spectroscopic observations are summarized in Table 3.

Figure 6 shows our full spectral series of SN 2024jlf. We find that SN 2024jlf exhibits features and evolution typical of SNe IIP: a mostly featureless blue continuum followed by prominent P Cygni lines of the hydrogen Balmer series and later of He. A broad $H\alpha$ profile first emerges in the +2.3-day SPRAT spectrum. $H\beta$ and bluer Balmer series lines become visible shortly afterward; the Binospec spectrum at +10.7 days shows P Cygni profiles in $H\alpha$, $H\beta$, $H\gamma$, $H\delta$, and possibly $H\epsilon$. He I $\lambda 5876$ is also visible in a P Cygni profile starting in the +9.6-day spectrum. Fe II absorption and the Ca near-infrared

²⁴ <https://www.not.iac.es/instruments/alfosc/>

²⁵ https://gitlab.com/steveschulze/pypeit_alfosc_env

²⁶ <https://kcwi-drp.readthedocs.io/>

²⁷ <https://github.com/PyWiFeS/pipeline>

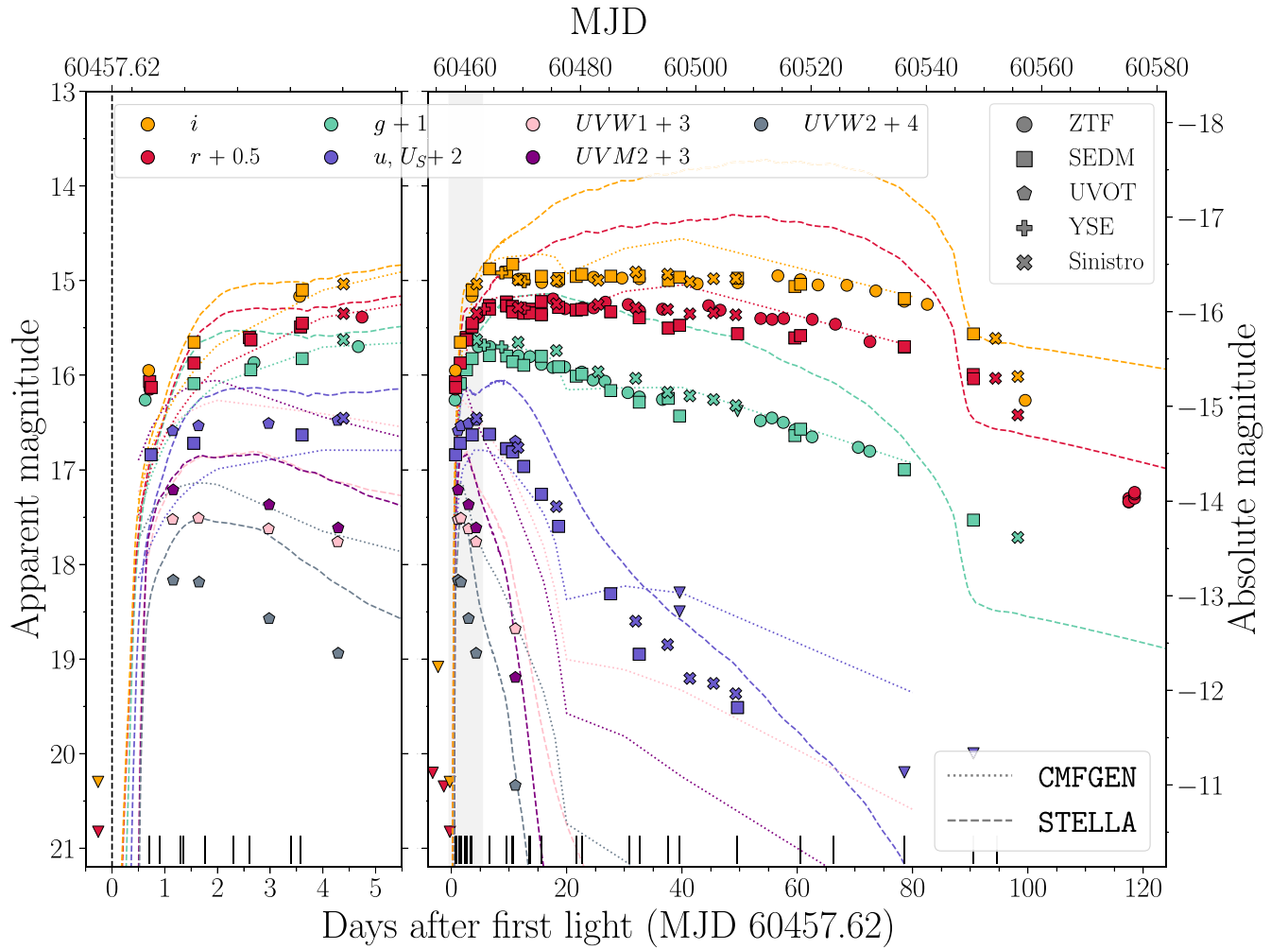


Figure 3. Multiband light curve of SN 2024jlf and best-fit model light curves. Left panel (and shaded region in right panel): SN 2024jlf rises exceptionally rapidly in all bands and begins to fade in the UV ~ 24 hr after t_{fl} (dashed black line). The STELLA model better reproduces the first 5 days after t_{fl} , but both models significantly underestimate the optical brightness ~ 24 hr after t_{fl} . Right panel: as a normal SN IIP, SN 2024jlf maintains near-peak luminosity for ~ 85 days before beginning to fade more rapidly. The CMFGEN model well reproduces the plateau luminosity across the optical bands, but the STELLA model strongly overestimates them.

triplet are visible starting around 3 weeks after first light. Model spectra, shown as gray lines, are discussed in Section 4.1.

Figure 7 shows the regions around main spectral lines in the early spectra of SN 2024jlf, which exhibit features characteristic of SNe II undergoing CSM interaction: He II $\lambda 4686$ and the ledge, C IV $\lambda\lambda 5801, 5812$, and H α . We also possibly detect narrow H β emission in the +0.9-day FLOYDS spectrum. He II is very common in flashing SNe, and its presence is often used to define an SN as flashing (e.g., D. Khazov et al. 2016; R. J. Bruch et al. 2021; B23). The ledge-shaped feature around 4450–4700 Å, visible in the first six epochs of spectroscopy, is typically interpreted as a sign of CSM interaction and has been seen in many interacting SNe, including SN 2013fs (O. Yaron et al. 2017) and others in the samples of B23 and JG24. Its origin is not precisely known, although it has been attributed to (i) a blend of high-ionization lines, including those of carbon, nitrogen, and oxygen (e.g., M. T. Soumagnac et al. 2020; R. J. Bruch et al. 2021; J. Pearson et al. 2023); (ii) high-velocity H β (e.g., A. Pastorello et al. 2006); and (iii) blueshifted He II $\lambda 4686$ (e.g., L. Dessart et al. 2017; C. Bullivant et al. 2018; N. N. Chugai & V. P. Utrobin 2023). See J. Pearson et al. (2023) for further discussion and references on the ledge feature.

Figure 8 shows that SN 2024jlf is also spectroscopically very similar to a number of previous events, selected from the class 3 sample in JG24. These other SNe (SN 2020xua, G. Terreran et al. 2020; SN 2021jtt, C. Angus et al. 2021; SN 2013fs, O. Yaron et al. 2017; SN 2020nif, D. Hiramatsu et al. 2020; SN 2020lfn, L. Izzo et al. 2020; SN 2021aaqn, K. Taggart et al. 2021) all show narrow He II, H α , and a variety of feature shapes in the region of the ledge. Most also show C IV emission (SN 2020xua, SN 2021jtt, SN 2021aaqn), and although it is not obvious in SN 2024jlf, nearly all others show narrow H β emission as well (SN 2020xua, SN 2021jtt, SN 2013fs, SN 2020lfn, and SN 2021aaqn).

The duration of flash/IIn-like features is key to constraining the extent of the dense CSM. B23 define the flash timescale τ as the duration for which the He II $\lambda 4686$ feature persists. The median τ in their golden flasher sample is 5.4 ± 2.7 days, including some events with $\tau \lesssim 2$ days. In all panels of Figure 7, we can clearly identify the narrow features in the +1.3-day spectra from SPRAT and ALFOOSC, and even earlier in the case of H α , but they all disappear by the +1.8-day WiFeS spectrum. We thus find $1.3 < \tau[\text{days}] < 1.8$. There appears to be a narrow H α feature in the +3.4-day SPRAT spectrum. In the Appendix (Figure 9), we confirm from the

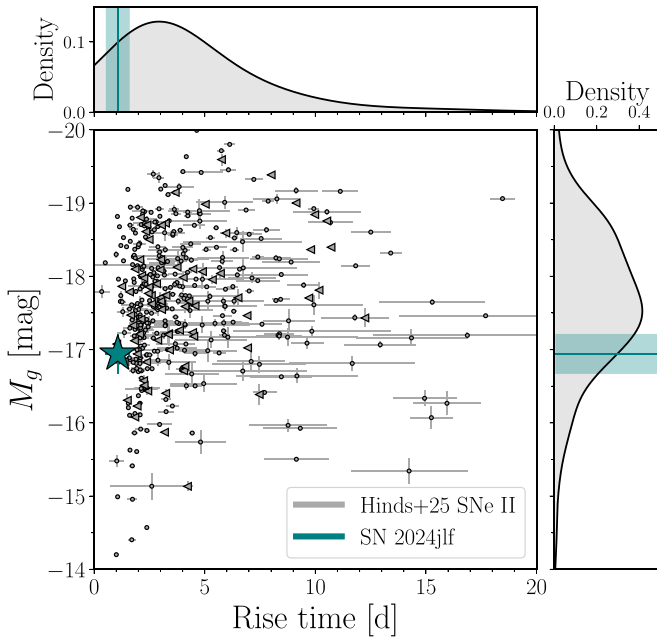


Figure 4. Comparison of SN 2024jlf (teal) g-band light-curve properties with those of an SN II sample (gray; Hinds et al. 2025, in preparation). SNe with poor light-curve coverage (see Hinds et al., for definition) only have upper limits on rise time, which are shown as arrowheads. SN 2024jlf rises quicker than $\sim 90\%$ of the sample despite peaking slightly fainter than average. Accelerated rise times are often seen in SNe II with CSM interaction.

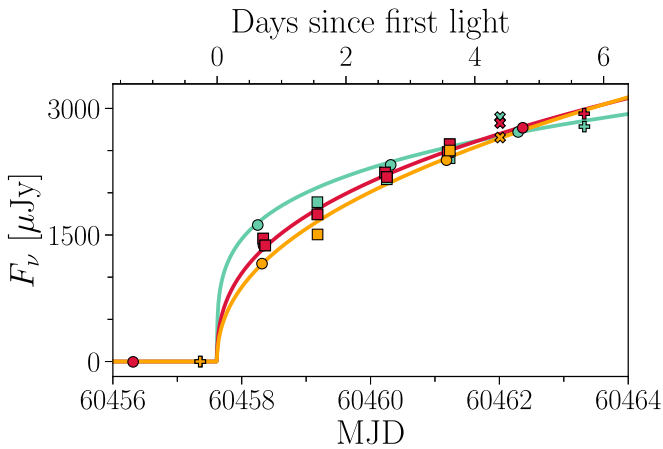


Figure 5. Joint power-law fits to the early *gri* photometry of SN 2024jlf (same colors and markers as in Figure 3) produce a time of first light estimate $t_{\text{fl}} = 60457.62 \pm 0.054$. Nondetections shortly before first light enable a precise estimation.

reduced 2D spectra that this is contamination from the host by modeling the SN and galaxy continua and inspecting the flux residuals. This contamination is not present in all SPRAT spectra because its presence and strength are dependent on the observing conditions and slit position of each observation.

JG24 define t_{lin} as the duration for which the narrow features show symmetric Lorentzian wings. This terminates once broad absorption profiles develop in the Balmer features, indicating that the CSM optical depth has decreased enough to allow the fastest-moving SN ejecta to emerge. The parameter t_{lin} is valuable because it is sensitive to the CSM density profile. The quality of our spectra and the strength of the flash features in SN 2024jlf do not, however, allow us to unambiguously identify when the Lorentzian wings subside.

Table 3
Spectroscopic Observations of SN 2024jlf

t_{obs} (MJD)	Phase (days)	Telescope/Instrument	R ($\lambda/\Delta\lambda$)	λ Range (Å)
60458.33	0.7	P60/SEDm	100	3770–9220
60458.53	0.9	FTN/FLOYDS-N	550	3350–10000
60458.91	1.3	LT/SPRAT	350	4000–8100
60458.97	1.3	NOT/ALFOSC	360	4000–9680
60459.39	1.8	ANU/WiFeS	3000	3200–9565
60459.93	2.3	LT/SPRAT	350	4000–8100
60460.23	2.6	P60/SEDm	100	3770–9220
60461.01	3.4	LT/SPRAT	350	4000–8100
60461.20	3.6	P60/SEDm	100	3770–9220
60464.20	6.6	P60/SEDm	100	3770–9220
60467.18	9.6	P60/SEDm	100	3770–9220
60468.22	10.6	P60/SEDm	100	3770–9220
60468.27	10.7	MMT/Binospec	1340	3820–9210
60471.18	13.6	P60/SEDm	100	3770–9220
60471.21	13.6	P60/SEDm	100	3770–9220
60473.20	15.6	P60/SEDm	100	3770–9220
60479.26	21.6	P60/SEDm	100	3770–9220
60480.21	22.6	P60/SEDm	100	3770–9220
60488.50	30.7	ANU/WiFeS	3000	3200–9565
60490.24	32.6	Keck/LRIS	1400	3100–5730
60490.24	32.6	Keck/LRIS	8500	5400–7050
60495.23	37.6	P60/SEDm	100	3770–9220
60497.18	39.6	P60/SEDm	100	3770–9220
60507.23	49.6	P60/SEDm	100	3770–9220
60518.17	60.6	P60/SEDm	100	3770–9220
60523.93	66.3	NOT/ALFOSC	360	4000–9680
60536.17	78.6	P60/SEDm	100	3770–9220
60548.15	90.5	P60/SEDm	100	3770–9220
60552.23	94.6	Keck/KCWI	900	3275–8925

Note. All spectra listed in this table are publicly available on the Weizmann Interactive Supernova Data Repository (WiSeREP).

(This table is available in machine-readable form in the [online article](#).)

When this is the case, JG24 scale the t_{lin} of a very similar SN with well-constrained t_{lin} (e.g., SN 2013fs) by the ratio of the epochs of the similar spectra (see Section 3.2 in JG24 for more details). This extrapolates the evolution of an event with very well constrained t_{lin} and assumes that it is proportionally consistent with that of the given SN. Following this procedure with our +1.3-day ALFOSC and the +1.9-day SN 2013fs spectrum (see Figure 8), we infer $t_{\text{lin}} = 0.96 \pm 0.34$ days for SN 2024jlf. Although this indirect inference is imperfect, it nonetheless appears to find a value consistent with the observations.

4. Matching with CMFGEN Models

We match our spectral series and UV/optical light curve of SN 2024jlf to models produced by L. Dessart et al. (2017) and L. Dessart & W. V. Jacobson-Galán (2023). Radiative hydrodynamics for these models were performed with the HERACLES code (M. González et al. 2007), and post-processing on specific HERACLES snapshots was performed with the radiative transfer code CMFGEN (D. J. Hillier & L. Dessart 2012).

The matching process involves comparing properties of the model and observed spectra: (i) which species are seen in narrow emission and their relative strengths, (ii) the duration

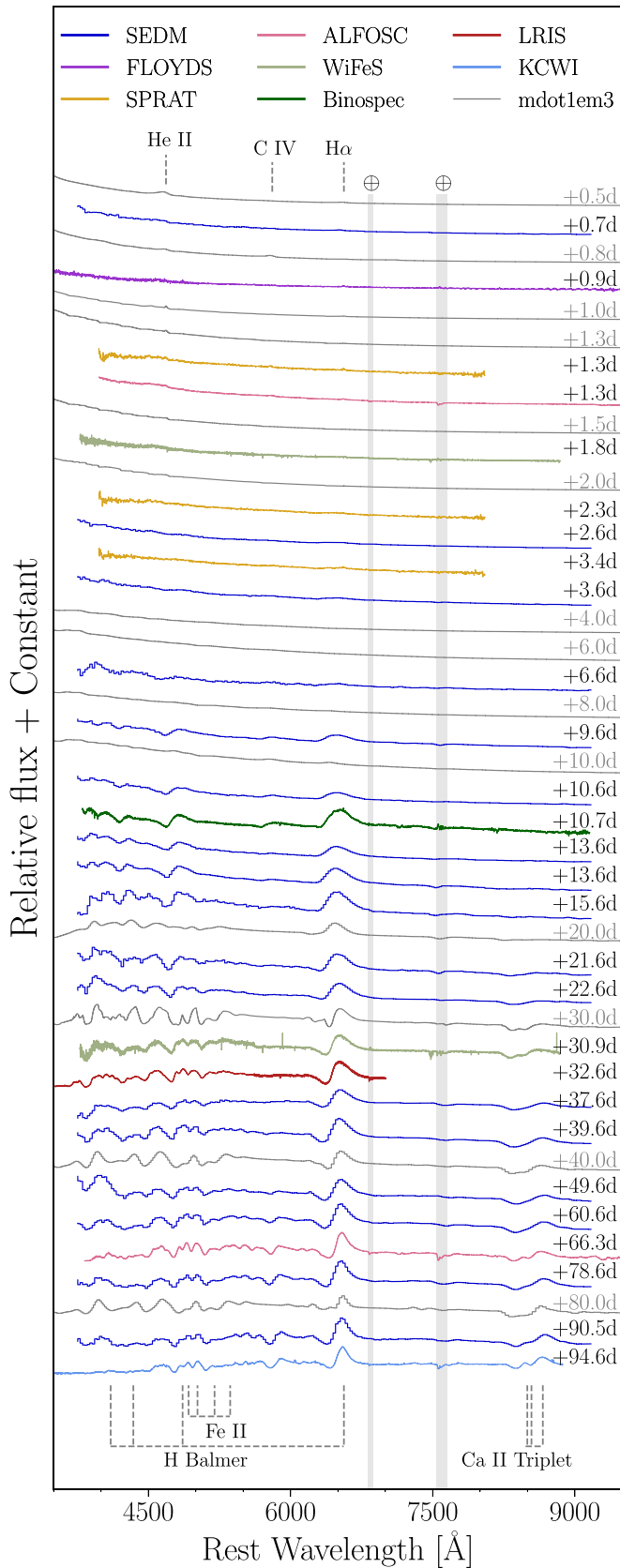


Figure 6. Full spectral series of SN 2024jlf (colored lines) and best-matched model spectra (gray lines). SN 2024jlf is a normal SN IIP showing flash features starting from a spectrum acquired just +0.7 days after t_n (see Figure 7). Over the next ~ 100 days, the SN develops features typical of SNe IIP, like broad Balmer series features.

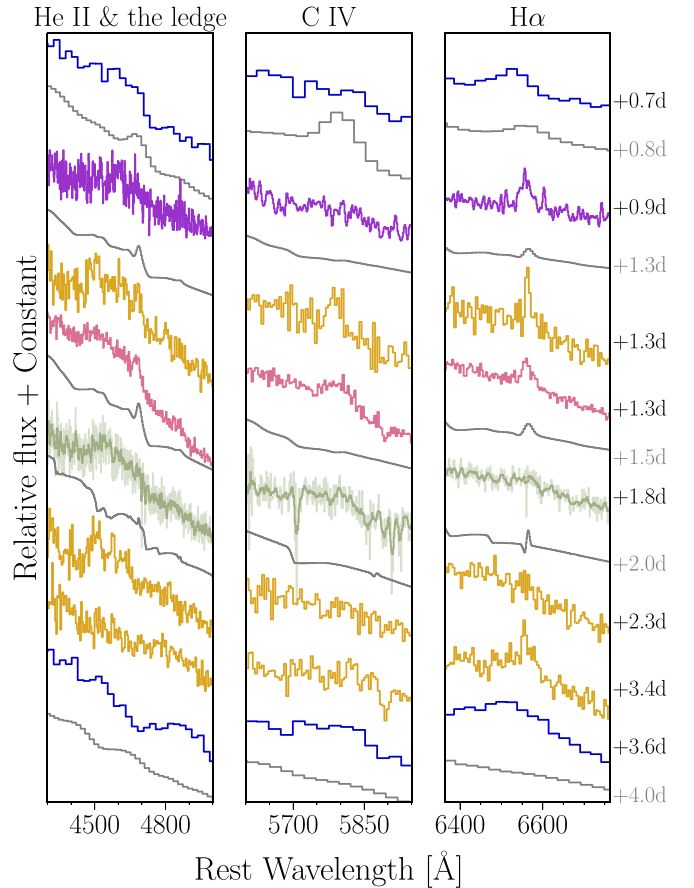


Figure 7. Early spectra of SN 2024jlf (colored lines) and best-matched model (gray lines) around regions showing flash features. He II, C IV, and possibly H β can be seen in narrow, short-lived emission. The WiFeS spectrum is shown unsmoothed (light green) and smoothed with a moving average filter (dark green) because it has greater noise around the important He II feature. All flash features, including He II, are present in the +1.3-day spectra but absent in the +1.8-day spectrum: $1.3 < \tau[\text{days}] < 1.8$.

of the flash features τ , and (iii) the relative phases of when typical SN IIP features (e.g., broad H α) develop. Because there are relatively few models (< 20) and they are quite heterogeneous across these three properties of interest, a quantitative search for the best-fit model is unnecessary. By visual inspection, we find that the `mdot1em3` model best matches the spectral properties of SN 2024jlf; its physical properties are discussed in Section 6.

4.1. Comparison to Model Spectra

We degrade the model spectra to facilitate comparison with observed spectra of varying spectral resolutions. This is done by convolving the model spectrum with a Gaussian kernel corresponding to the spectral resolution of the observed spectrum nearest in phase to the model spectrum. This process, as well as its effect on the visibility of narrow features in the ultra-low-resolution SEDM spectra ($R \sim 100$), is discussed in depth in B23. We also scale the continuum of the early (phase < 10 days) model spectra to match that of the nearest observed spectrum; this is not necessary for any of the later spectra.

Figure 7 compares the early spectral series of SN 2024jlf (colored lines) with that of `mdot1em3` (gray lines). The

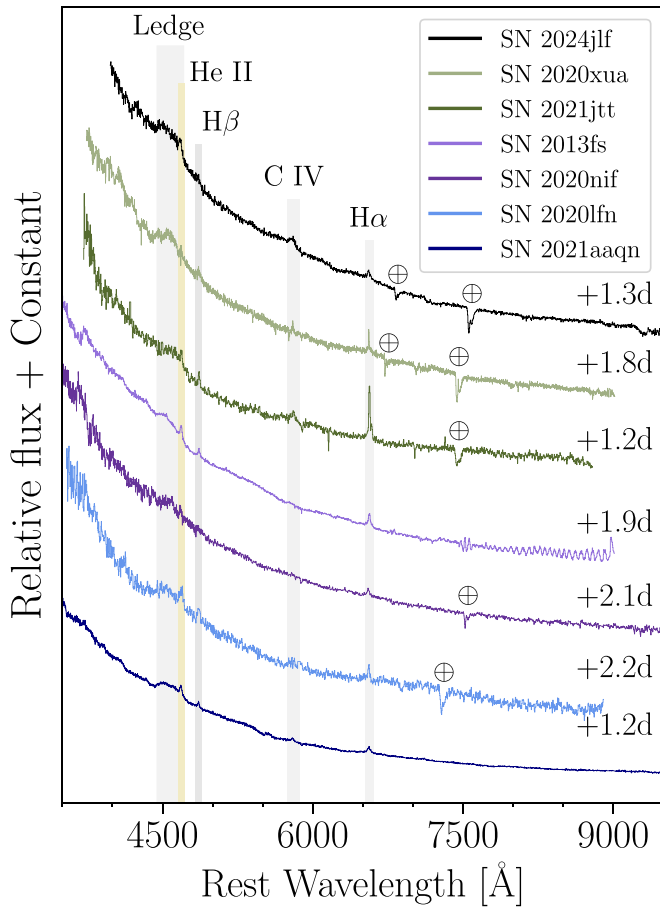


Figure 8. Comparing SN 2024jlf and spectroscopically similar SNe from the JG24 class 3 sample. All show narrow emission in He II, H α , and some additional emission feature(s) in the region of the ledge. Most events also have narrow C IV and/or H β emission.

model spectra show flash features in He II, C IV, and H α , as do the observed spectra, and no additional flash features appear in the model spectra. We find $2 < \tau[\text{days}] < 4$ for mdot1em3, which is nearly consistent with our constraints on τ for SN 2024jlf: $1.3 < \tau[\text{days}] < 1.8$. The primary deviation between the observations and the model is that the model only develops a broad H α feature after ~ 10 days, while we observe a similar feature emerging in the +2.3-day spectrum of SN 2024jlf (see Figure 6).

There are minor deviations between the model spectra and the observations: (i) The +0.8-day model spectrum shows a narrow He II feature and no ledge, while the +0.7-day SEDM spectrum shows a ledge without obvious narrow He II. (ii) The model’s C IV feature is prominent starting from +0.8 days despite not being visible until +1.3 days in SN 2024jlf. (iii) The +0.7-day SEDM spectrum shows blueshifted H α , while the model shows no such shift. SN 2023ixf also showed a blueshifted H α profile in early high-resolution spectroscopy (D. Dickinson et al. 2025), although the shift only developed days after t_{fl} . Higher-resolution spectroscopy would have been necessary to further investigate this feature. Despite these differences, all of the key features (He II, C IV, and H α) disappear on similar timescales in the model and observations, and some of the discrepancies could be explained by insufficient signal in the observations.

Across our full spectral series (see Figure 6), no other major deviations are apparent. The model well reproduces the

Balmer series features and, once they appear, the Fe II and Ca II lines.

4.2. Comparison to Model Photometry

The corresponding model light curve (dotted lines) is compared to that of SN 2024jlf (points) in Figure 3. The left panel makes clear that mdot1em3 rises far slower in the optical and near-UV ($griU_S$) than SN 2024jlf. The optical bands are all underestimated through the first 7 days after t_{fl} . In the UV bands (UVW1, UVM2, UVW2), however, this pattern is reversed; mdot1em3 initially rises quicker than SN 2024jlf and uniformly overestimates the UV flux. After the initial rapid UV rise, mdot1em3 then peaks later in the (near-)UV bands than SN 2024jlf.

The right panel shows that peak luminosity is achieved at a very similar phase in the optical bands. The r and i bands are exceptionally well fit beyond ~ 10 days after t_{fl} , but the g -band light curve of mdot1em3 slightly overestimates the SN flux by ~ 0.2 mag across the plateau. As was apparent in the early light curve, the UV flux from SN 2024jlf is strongly overestimated by the model. Although the initial UV rise in mdot1em3 is quicker than observed, the decline rate of the model is slower than observed.

The aspects of disagreement between the model and observations cannot be reconciled by changing the amount of host attenuation we correct for. Decreasing the $A_{V,\text{host}}$ from 0.636 to 0.4 causes the gri bands to fit well from 3 days after t_{fl} onward, but the early rise rate is still poorly reproduced and the overestimations in the near-UV and UV are significantly worsened. Increasing $A_{V,\text{host}}$ to 0.8 makes the UVM2 and UVW2 bands fit well between 2 and 5 days after t_{fl} , but (i) UVW1 is still overestimated, (ii) the fit to the early optical rise is worsened, and (iii) the overestimates in the near-UV and g bands are greater.

5. Matching with STELLA Models

We also compare the observations with a grid of $\sim 228,000$ SN II models from T. J. Moriya et al. (2023). These models are produced with the one-dimensional radiation hydrodynamics code STELLA (S. I. Blinnikov et al. 1998, 2006; S. Blinnikov et al. 2000) and adopt RSG progenitor models from T. Sukhbold et al. (2016). Although the models do produce SEDs well sampled in time, the SEDs do not have sufficient wavelength resolution to compare against observed spectra. For this reason, only light curves are available to compare against observations.

The models in the T. J. Moriya et al. (2023) grid exhibit an artifact in the early light curve delaying first light. This artifact arises from the initial condition of the numerical simulation wherein photons diffuse out of the CSM before the shock breakout. The “zero” phase in these model light curves is the time at which thermal energy is injected into the simulation, but the actual shock breakout happens roughly 1–3 days later. T. J. Moriya & A. Singh (2024) handle this by recalculating the goodness-of-fit metric for each model by iterating through a grid of small adjustments to the provided phases. Instead, we compute offsets between the provided zero epoch and the time of first light t_{fl} by identifying when the light curve begins its primary brightening phase. These offsets are applied to the phases of the model’s photometry, so that we can fix t_{fl} before computing goodness-of-fit metrics. We evaluate the fit of each

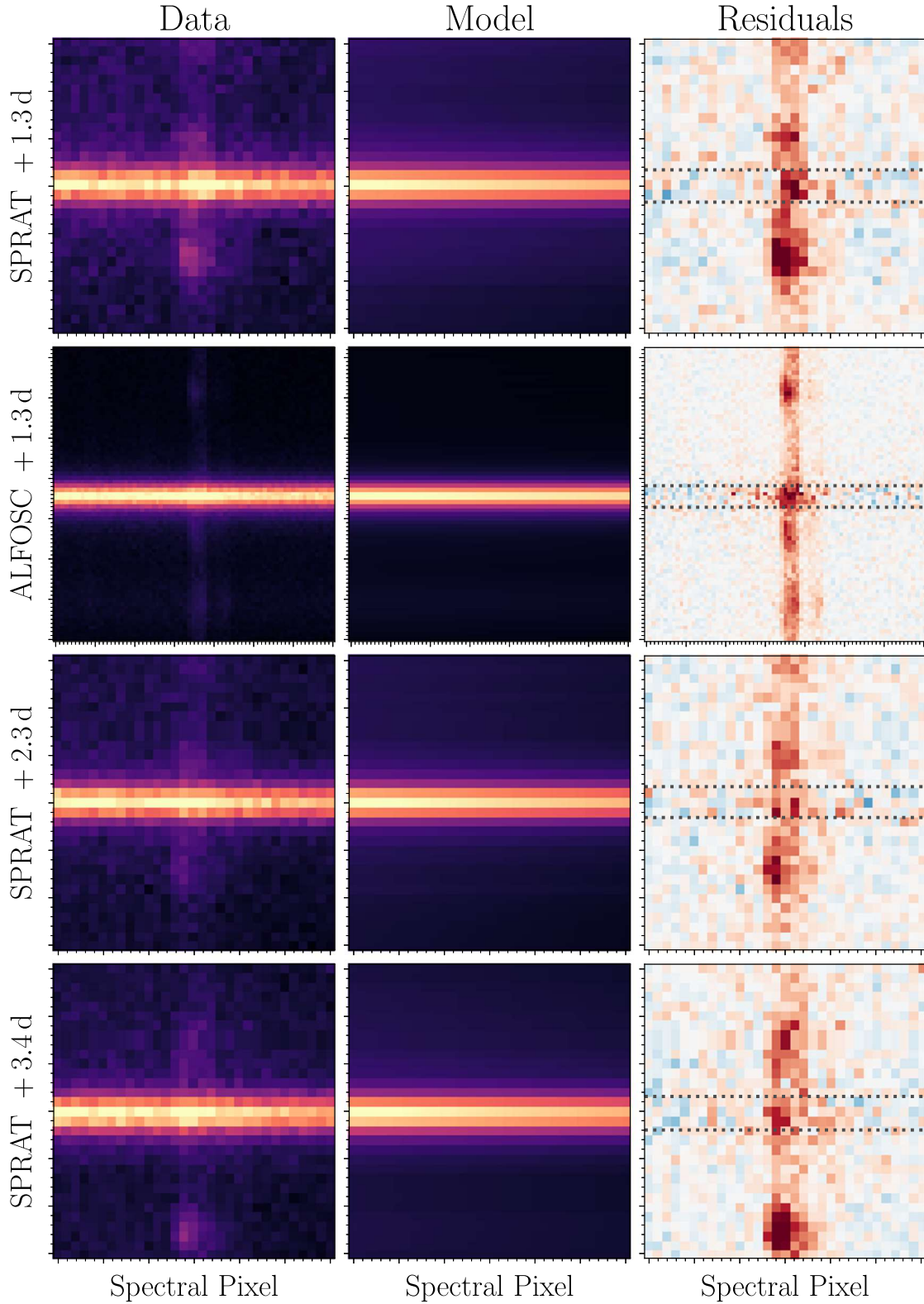


Figure 9. The disappearance of the $H\alpha$ flash feature viewed from early 2D spectra. Left column: the calibrated 2D spectra in the vicinity of the $H\alpha$ emission; middle column: models of the SN continua and the global background, including the host galaxy continua and the sky background (see the text for modeling details); right column: flux residuals originating from narrow SN and host emission lines, with the FWHM of the SN trace overlaid (dotted lines). Each cutout spans $\sim 150 \text{ \AA}$ in spectral direction (centered at 6600 \AA) and $\sim 14''$ in spatial direction. The host galaxy is spatially resolved along the slit, and the vertical stripes in the left and right columns correspond to $H\alpha$ emission from star-forming regions covered by the slit. Each observation was made with the slit placed at a specific, different position angle; thus, the $H\alpha$ patterns along the slit direction vary between observations. At +1.3 days, there is residual flux centered within the FWHM of the SN but shifted ~ 1 pixel rightward of the host emission's centroid. This indicates the existence of a slightly redshifted ($\sim 10^2 \text{ km s}^{-1}$) component intrinsic to the SN. There is no evidence for such a component in the +2.3-day and +3.4-day spectra, indicating the disappearance of narrow $H\alpha$ emission from the SN.

model to the observed g-band light curve by computing the χ^2 statistic, which quantifies the agreement between the model light curve and the observed data. This model-fitting approach quantifies how well each model reproduces the observed light curve while accounting for observational uncertainties. Models are ranked based on their χ^2 values, with a lower χ^2 indicating a better agreement. This approach enables a quantitative ranking of the $\sim 228,000$ models in the grid. The physical properties of the best-fit model are discussed in Section 6.²⁸

The best-fit model does not capture SN 2024jlf's exceptionally rapid optical and near-UV rise in the first ~ 24 hr after t_{R} . From 2 to 7 days, however, the optical and near-UV light curves are quite well matched. The UV flux is underestimated in the first epoch of Swift/UVOT photometry, but the decline rate is well matched by the final epoch.

The optical flux during the plateau, ~ 7 days after t_{R} and onward, is overestimated. The brighter plateau light curves from the T. J. Moriya et al. (2023) grid can be attributed to the progenitor models derived by T. Sukhbold et al. (2016), combined with the inherent degeneracies in light-curve modeling (J. A. Goldberg et al. 2019). The progenitors are evolved employing a low mixing-length parameter, leading to systematically larger progenitor radii for a given zero-age main-sequence (ZAMS) mass, which enhances the recombination radius and increases the plateau brightness (T. J. Moriya & A. Singh 2024). In addition, ^{56}Ni being mixed to half of the H envelope in the progenitor models of T. Sukhbold et al. (2016) leads to a brighter plateau. This is because ^{56}Ni starts diffusing out much earlier than the end of the plateau phase, as was seen in SN 2016gfy (A. Singh et al. 2019). The combination of these effects causes the model's optical light curves, particularly in the redder bands, to peak later than observed. In fact, the modeled peaks occur after the observed peaks across all bands. Although other models in the T. J. Moriya et al. (2023) grid better match the flux on the plateau, we prefer this model, as it fits the rise better than any others. The CSM interaction most significantly influences the rise and the UV light curves, so this model should provide the best estimate of the CSM properties.

Since the models from T. J. Moriya et al. (2023) extend past the end of the plateau, we can assess their fit of the plateau duration and the ^{56}Co tail. The best-fit model's plateau is ~ 10 days shorter than that of SN 2024jlf, and the model's r-band tail flux is within ~ 0.2 mag of the ZTF photometry $+120$ days after t_{R} .

We modulate the amount of host attenuation as an attempt to improve the match. Increasing $A_{V,\text{host}}$ to 0.9 causes the near-UV and g-band flux to match the model very well beyond ~ 10 days after t_{R} , but doing so (i) ruins the previously good fit to the optical data between 24 and 72 hr after t_{R} , (ii) causes the UV to be systematically and significantly underestimated, and (iii) does not alleviate the poor fit to the ri-band plateau flux. Decreasing $A_{V,\text{host}}$ worsens nearly all aspects of the match. We conclude that alternative values of $A_{V,\text{host}}$ do not provide a significantly better match between this model and our observations.

6. Discussion

We have matched observations of SN 2024jlf to models from grids produced by two different radiative hydrodynamics

codes. Here we compare the ability of the best-matched models from these very different grids to reproduce the observed properties of SN 2024jlf and compare the physical properties inferred from the models.

6.1. Comparison of Model Fits

We compare only the models' ability to reproduce the photometry and not the spectroscopy because the STELLA SEDs are not of sufficient wavelength resolution to compare against observations.

Neither model better reproduces the entire optical light curve than the other model. The best-matched STELLA model much better recovers the early optical light-curve behavior; the optical is very well reproduced from 1.5 to 6 days. At similar phases, the best-matched CMFGEN model is still rising and underestimates the optical and near-UV flux. Beyond ~ 6 days, the STELLA model diverges from the observations and far overestimates the plateau flux, while the CMFGEN model reproduces the plateau well.

The UV light curve, particularly at early times, is most important, as it is likely dominated by flux excess originating from the CSM interaction. In this domain, neither model matches the observations very well; however, the STELLA model better traces the evolution, especially beyond ~ 4 days after t_{R} . The CMFGEN model overestimates the UV flux across all bands and all epochs of UV photometry.

6.2. Physical Parameter Inference from Model Matches

The key progenitor and CSM parameters of interest are the mass-loss rate (\dot{M}) and the CSM density profile (ρ_{CSM}). Both models adopt density profiles that exponentially decline from the surface of the star outward. The T. J. Moriya et al. (2023) grid parameterizes the CSM structure as β and includes models where the density decreases sharply at the surface of the star when transitioning into the CSM (smaller β) and models where the density decays as a roughly continuous exponential from within the star to beyond 10^{15} cm (large β ; see Figure 1 in T. J. Moriya et al. 2023). The best-matched STELLA model uses the most gradually declining CSM density profile for the selected progenitor star ZAMS mass M_* , which corresponds to $\beta = 5.0$ or $\rho \propto r^{-1.674}$. The CMFGEN model's density profile declines more rapidly ($\rho \propto r^{-3.174}$), indicating that the matter in the CSM is concentrated closer to the star.

The best-matched models infer a mass-loss rate consistent with other SNe exhibiting similar spectroscopic features. The best-matched CMFGEN model has $\dot{M} = 10^{-3} M_{\odot} \text{ yr}^{-1}$, while the best-matched STELLA model has $\dot{M} = 10^{-4} M_{\odot} \text{ yr}^{-1}$. These values roughly agree with mass-loss rates of SNe in Figure 8 inferred in JG24 using CMFGEN models. Furthermore, the difference of an order of magnitude is not concerning because the model grids do not provide fine granularity in values of \dot{M} . Based on spectra from CMFGEN models with greater ($\dot{M} \geq 10^{-2} M_{\odot} \text{ yr}^{-1}$) or smaller ($\dot{M} \leq 10^{-5} M_{\odot} \text{ yr}^{-1}$) mass-loss rates, we can also confidently rule out those ranges of \dot{M} . Models with much larger \dot{M} tend to show stronger and additional narrow emission features with greater durations; models with much smaller \dot{M} show little to no narrow emission features.

The duration of enhanced mass loss ($t_{\dot{M}}$) can be inferred from the shock velocity, the duration of IIn-like features, and the wind velocity: $t_{\dot{M}} = v_{\text{sh}} t_{\text{IIn}} / v_{\text{w}}$. To make this inference, we

²⁸ The best-fit model is named s10ni0p04hm6_m4.0b5.0r8e14e15.

adopt the indirectly inferred t_{lin} from Section 3.4 ($t_{\text{lin}} = 0.96 \pm 0.34$ days). We also use the expansion velocity measured from the blue edge of the $H\alpha$ absorption as a lower limit for the shock velocity, which yields $v_{\text{sh}} \geq 18,000 \text{ km s}^{-1}$ from the Keck/LRIS spectrum. This cannot be precisely measured from earlier spectra, as they do not show a broad $H\alpha$ feature, are not of sufficient resolution, or, in the case of the Binospec spectrum, exhibit blending between $H\alpha$ and Si II . The t_M also depends on the wind velocity, which varies between the models: $v_w = 50 \text{ km s}^{-1}$ for CMFGEN and $v_w = 10 \text{ km s}^{-1}$ for STELLA. These values produce a lower limit on the duration of enhanced mass loss: assuming CMFGEN v_w , $t_M \geq 3.0 \times 10^7 \text{ s} \approx 1 \text{ yr}$; assuming STELLA v_w , $t_M \geq 1.5 \times 10^8 \text{ s} \approx 5 \text{ yr}$.

Matching to the extremely large T. J. Moriya et al. (2023) grid also provides suggestions for the values of additional progenitor and explosion properties like the mass of ^{56}Ni (M_{Ni}), the progenitor star ZAMS mass (M_*), and the explosion energy (E). L. Dessart & W. V. Jacobson-Galán (2023) do not consider varying these parameters, as their study is conducted to qualitatively reproduce IIn-like features.

The best-matched STELLA model adopts $M_{\text{Ni}} = 0.04 M_\odot$, $M_* = 10 M_\odot$, and $E = 1.5 \times 10^{51} \text{ erg}$. Models with higher explosion energies ($E \gtrsim 3 \times 10^{51} \text{ erg}$) tend to better reproduce the rapid rise observed in SN 2024jlf but are associated with significantly brighter plateaus. Our best-matched model represents a compromise, balancing the need to match both the rise time and the plateau brightness.

The M_* of the best-matched model, which controls the duration of the plateau, is the smallest value considered in the grid. The progenitor models adopted from T. Sukhbold et al. (2016) by the T. J. Moriya et al. (2023) grid couple the progenitor mass and radius. Thus, this is not a conclusive inference because there are degeneracies between ejecta mass, radius, and explosion energy (J. A. Goldberg et al. 2019). These inferred properties should be interpreted as one plausible solution, rather than a unique configuration.

Lastly, we reiterate that none of the models in either grid reproduce all observed properties of SN 2024jlf. Both best-matched models underestimate the earliest epochs of optical and near-UV photometry by ~ 1 mag.

6.3. The Future of BTSbot-nearby and Rapid, Autonomous Follow-up

BTSbot-nearby is the latest in a rich history of rapid transient follow-up efforts conducted following discoveries by the Palomar 48-inch telescope. Whether for infant SNe or gamma-ray bursts, collecting valuable data shortly after transient discovery has long been a core science goal of these programs (S. B. Cenko et al. 2006; M. J. Graham et al. 2019). Most recently and most closely related to BTSbot-nearby, auto-triggering technology was developed in the AMPELbroker (J. Nordin et al. 2019), with SNGuess (N. Miranda et al. 2022) being used to select targets for follow-up. Automation of transient identification and follow-up, as demonstrated with BTSbot-nearby, is a necessary advancement to previous efforts to minimize latency and collect the earliest possible data.

Further minimization of latency from the current state of BTSbot-nearby would be very challenging. The limited sensitivity of ZTF aside, one of the greatest remaining sources of latency is the requirement of two detections before

triggering follow-up to reject moving objects. The ZTF cadence and scheduling tend to make the latency associated with this criterion $\gtrsim 1$ hr. If the BTSbot-nearby filtering were improved to be able to reject moving objects (i.e., asteroids and satellites), the typical latency could be reduced. Section 5.3 of N. Rehemtulla et al. (2024b) illustrates that a program of this sort could have expedited the follow-up of SN 2023ixf by ~ 10 hr. Nevertheless, such aggressive follow-up remains impossible in the vast majority of cases.

BTSbot-nearby now regularly triggers target-of-opportunity (ToO) requests to SEDM and aids in the collection of very early follow-up data. In the case of SN 2025ay, BTSbot-nearby discovered the transient (N. Rehemtulla et al. 2025) and collected a spectrum with SEDM just 23 minutes later. The scientific value of the data, irrespective of how early it may be taken, is limited by the data quality. This was a major challenge in B23, where SEDM data often left it ambiguous whether or not narrow He II emission lines were present. Another future advancement for BTSbot-nearby lies in triggering larger telescopes equipped with more capable instruments. BTSbot-nearby is already capable of triggering new urgency 0 ToOs to Swift/UVOT (A. Tohuvavohu et al. 2024), as well as triggers to the 4.1 m Southern Astrophysical Research telescope through the Astronomical Event Observatory Network (AEON; R. A. Street et al. 2020) integration in Fritz/SkyPortal.

Automation of transient workflows can also act as a service to the community. In the end-to-end automated BTS workflow (N. Rehemtulla et al. 2023), new transients are reported to TNS by BTSbot and classifications are reported by SNIa-score (C. Fremling et al. 2021) and pySEDM (M. Rigault et al. 2019). Making these data and findings available publicly and quickly enables timely follow-up by others in the community. This is being expanded to CCSNe with the use of CCSNscore (Y. Sharma et al. 2025). Moreover, this practice synergizes very well with BTSbot-nearby: very early spectra made publicly available immediately can then motivate follow-up with larger facilities by anyone in the community.

7. Summary

We have presented the new BTSbot-nearby program, which discovered the 18.5 Mpc SN IIP SN 2024jlf and obtained spectroscopic follow-up just $+0.7$ days after first light (Section 3.1). BTSbot-nearby autonomously triggers ToOs for new transients identified by the BTSbot model that are coincident with nearby ($D < 60$ Mpc) galaxies (Section 2).

The early spectra of SN 2024jlf reveal flash ionization features in $H\alpha$, C IV, and He II, which persist for $1.3 < \tau [\text{days}] < 1.8$ (Section 3.4). With deep nondetections shortly prior to first light, we find that SN 2024jlf rises exceptionally rapidly, quicker than 90% of SNe II in a large ZTF sample (Section 3.3). SN 2024jlf later appears as a normal SN IIP with an ~ 85 -day plateau phase and broad, prominent Balmer P Cygni features.

We match our observations to model grids produced by two independent radiation hydrodynamics codes. The best-matched CMFGEN model well reproduces our spectral series and the plateau phase optical brightness, although it systematically overestimates the UV flux (Section 4). The best-matched STELLA model much better reproduces the early and UV photometry despite dramatically overestimating the plateau

phase optical brightness (Section 5). Either model is associated with physical parameters, which can provide suggestions to the nature of SN 2024jlf's RSG progenitor (Section 6). The mass-loss rates inferred from either model are roughly consistent: $\dot{M} = 10^{-3} M_{\odot} \text{ yr}^{-1}$ from the CMFGEN model and $\dot{M} = 10^{-4} M_{\odot} \text{ yr}^{-1}$ from the STELLA model. Moreover, models with larger or smaller \dot{M} are clearly disfavored in both grids, so we infer $10^{-4} < \dot{M} [M_{\odot} \text{ yr}^{-1}] < 10^{-3}$. Based on adopted values of wind velocity by either model, they suggest that the enhanced mass-loss phase persists for $1 < t_{\dot{M}} [\text{yr}] < 5$.

These findings demonstrate the value of automated ToO follow-up of transients for probing the nature of flash ionization in CCSNe. Automating first-response follow-up to the initial discovery of a young transient can provide the opportunity to collect data at otherwise inaccessible phases of the transient's evolution.

Acknowledgments

W. M. Keck Observatory, MMT Observatory, and Zwicky Transient Facility access for N.R., A.A.M., S.S., and C.L. was supported by Northwestern University and the Center for Interdisciplinary Exploration and Research in Astrophysics (CIERA).

The material contained in this document is based on work supported by a National Aeronautics and Space Administration (NASA) grant or cooperative agreement. Any opinions, findings, conclusions, or recommendations expressed in this material are those of the author and do not necessarily reflect the views of NASA. This work was supported through a NASA grant awarded to the Illinois/NASA Space Grant Consortium.

This research was supported in part through the computational resources and staff contributions provided for the Quest high-performance computing facility at Northwestern University, which is jointly supported by the Office of the Provost, the Office for Research, and Northwestern University Information Technology.

Based on observations obtained with the Samuel Oschin Telescope 48 inch and the 60 inch Telescope at the Palomar Observatory as part of the Zwicky Transient Facility project. ZTF is supported by the National Science Foundation under grants Nos. AST-1440341 and AST-2034437 and a collaboration including current partners Caltech, IPAC, the Oskar Klein Center at Stockholm University, the University of Maryland, University of California, Berkeley, the University of Wisconsin–Milwaukee, University of Warwick, Ruhr University, Cornell University, Northwestern University, and Drexel University. Operations are conducted by COO, IPAC, and UW.

The Young Supernova Experiment is supported by the National Science Foundation through grants AST-1518052, AST-1815935, AST-1852393, AST-1911206, AST-1909796, and AST-1944985; the David and Lucile Packard Foundation; the Gordon & Betty Moore Foundation; the Heising-Simons Foundation; NASA through grants NNG17PX03C, 80NSSC19K1386, and 80NSSC20K0953; the Danish National Research Foundation through grant DNR132; VILLUM FONDEN Investigator grants 16599, 10123, and 25501; the Science and Technology Facilities Council through grants ST/P000312/1, ST/S006109/1, and ST/T000198/1; the Australian Research Council Centre of Excellence for All Sky

Astrophysics in 3 Dimensions (ASTRO 3D) through project no. CE170100013; the Hong Kong government through GRF grant HKU27305119; the Independent Research Fund Denmark via grant Nos. DFF 4002-00275 and 8021-00130; and the European Union's Horizon 2020 research and innovation program under the Marie Skłodowska-Curie through grant No. 891744.

The Pan-STARRS1 Surveys (PS1) and the PS1 public science archive have been made possible through contributions by the Institute for Astronomy, the University of Hawaii, the Pan-STARRS Project Office, the Max-Planck Society and its participating institutes, the Max Planck Institute for Astronomy, Heidelberg and the Max Planck Institute for Extraterrestrial Physics, Garching, Johns Hopkins University, Durham University, the University of Edinburgh, the Queen's University Belfast, the Harvard-Smithsonian Center for Astrophysics, the Las Cumbres Observatory Global Telescope Network Incorporated, the National Central University of Taiwan, the Space Telescope Science Institute, the National Aeronautics and Space Administration under grant No. NNX08AR22G issued through the Planetary Science Division of the NASA Science Mission Directorate, the National Science Foundation grant No. AST-1238877, the University of Maryland, Eotvos Lorand University (ELTE), the Los Alamos National Laboratory, and the Gordon and Betty Moore Foundation.

YSE computations are aided by the University of Chicago Research Computing Center, the Illinois Campus Cluster, and facilities at the National Center for Supercomputing Applications at UIUC.

Observations reported here were obtained at the MMT Observatory, a joint facility of the University of Arizona and the Smithsonian Institution.

The authors wish to recognize and acknowledge the very significant cultural role and reverence that the summit of Maunakea has always had within the indigenous Hawaiian community. We are most fortunate to have the opportunity to conduct observations from this mountain.

SED Machine is based on work supported by the National Science Foundation under grant No. 1106171. The ZTF forced-photometry service was funded under Heising-Simons Foundation grant No. 12540303 (PI: Graham). The Gordon and Betty Moore Foundation, through both the Data-Driven Investigator Program and a dedicated grant, provided critical funding for SkyPortal.

Based on observations made with the Nordic Optical Telescope, owned in collaboration by the University of Turku and Aarhus University, and operated jointly by Aarhus University, the University of Turku, and the University of Oslo, representing Denmark, Finland, and Norway; the University of Iceland; and Stockholm University at the Observatorio del Roque de los Muchachos, La Palma, Spain, of the Instituto de Astrofísica de Canarias.

N.R., C.L., and A.A.M. are supported by DoE award No. DE-SC0025599. W.J.-G. is supported by NASA through the NASA Hubble Fellowship grant HSTHF2-51558.001-A awarded by the Space Telescope Science Institute, which is operated by the Association of Universities for Research in Astronomy, Inc., for NASA, under contract NAS5-26555. Parts of this research were supported by the Australian Research Council Centre of Excellence for Gravitational Wave Discovery (OzGrav), through project no. CE230100016 and

the Australian Research Council Discovery Early Career Researcher Award (DECRA) through project no. DE230101069. M.W.C acknowledges support from the National Science Foundation with grant Nos. PHY-2308862 and PHY-2117997. D.O.J. acknowledges support from NSF grants AST-2407632 and AST-2429450, NASA grant 80NSSC24M0023, and HST/JWST grants HST-GO-17128.028, HST-GO-16269.012, and JWST-GO-05324.031, awarded by the Space Telescope Science Institute (STScI), which is operated by the Association of Universities for Research in Astronomy, Inc., for NASA, under contract NAS5-26555. S.R.K. thanks the Heising-Simons Foundation for supporting his research.

This research has made use of NASA’s Astrophysics Data System. This research has made use of the NASA/IPAC Extragalactic Database, which is funded by the National Aeronautics and Space Administration and operated by the California Institute of Technology.

Software citation information aggregated using the Software Citation Station (T. Wagg & F. S. Broekgaarden 2024; T. Wagg et al. 2024).

Facilities: PO:1.2m (ZTF), PO:1.5m (SEDM), Liverpool:2m (SPRAT), MMT (Binospec), NED, NOT (ALFOSC), Keck:I (LRIS), Keck:II (KCWI), ATT (WiFeS).

Software: *astropy* (Astropy Collaboration et al. 2013, 2018, 2022), *Jupyter* (F. Perez & B. E. Granger 2007; T. Kluyver et al. 2016), *Keras* (F. Chollet et al. 2015), *matplotlib* (J. D. Hunter 2007), *NASA/IPAC Extragalactic Database (NED)* (2019), *numpy* (C. R. Harris et al. 2020), *pandas* (W. McKinney 2010; The pandas development team 2024), *penquins* (D. Duev et al. 2021), *python* (G. Van Rossum & F. L. Drake 2009), *scipy* (W. McKinney 2010; P. Virtanen et al. 2020; R. Gommers et al. 2024), *astroquery* (A. Ginsburg et al. 2019; A. Ginsburg et al. 2024), *Cython* (S. Behnel et al. 2011), *dustmaps* (G. Green 2018; G. Green et al. 2024), *h5py* (G. Green 2018; G. Green et al. 2024), *SkyPortal* (S. J. van der Walt et al. 2019; M. W. Coughlin et al. 2023), *tensorflow* (M. Abadi et al. 2015), *tqdm* (C. da Costa-Luis 2019), and the *Weights and Biases* platform (L. Biewald 2020). The *BTSbot-nearby* alert filter in MongoDB aggregation pipeline syntax and additional utilities for testing it can be found at <https://github.com/nabeelre/BTSbot-nearby-utils>.

Appendix

Disentangling Flash Features from the Host Emission

Emission lines (e.g., $H\alpha$) from the host galaxy can contaminate the SN spectrum, and it is critical (and often not trivial) to disentangle flash features of the SN from the host emission. To precisely determine when the $H\alpha$ flash feature disappears, in Figure 9 we present the 2D spectra obtained before +3.4 days with LT/SPRAT and NOT/ALFOSC, which encode the spatial distribution of $H\alpha$ emission from the host. The calibrated 2D spectra all exhibit a vertical stripe that overlaps the horizontal trace of the SN continuum, corresponding to the $H\alpha$ emission from star-forming regions in the host galaxy covered by the slit. Because the slit was oriented at a different position angle for each observation, the $H\alpha$ background varies over observations. In the vicinity of the $H\alpha$ features ($\sim 150 \text{ \AA}$ as displayed in the image cutouts), we assume (i) that the flux density of the SN continuum can be approximated with a linear function of wavelength and (ii) that

the PSF of the SN remains the same at different wavelengths. The contribution of the SN continuum at pixel $(x_{\text{spec}}, x_{\text{spat}})$ is

$$F_{\text{SN,con}}(x_{\text{spec}}, x_{\text{spat}}) = (k_{\text{SN}}x_{\text{spec}} + b_{\text{SN}}) \cdot \text{PSF}(x_{\text{spat}}). \quad (\text{A1})$$

We estimate the PSF using data outside an $l_{\text{mask}} = 15$ -pixel mask covering the spectral pixels contaminated by the $H\alpha$ emission. At each x_{spat} we have

$$\text{PSF}(x_{\text{spat}}) = \frac{\text{Median}_{|x_{\text{spec}} - x_{H\alpha}| > l_{\text{mask}}/2}}{\sum_{x_{\text{spat}}} \left[\frac{F_{\text{obs}}(x_{\text{spec}}, x_{\text{spat}}) - F_{\text{sky}}(x_{\text{spec}}, x_{\text{spat}})}{\sum_{x_{\text{spat}}} [F_{\text{obs}}(x_{\text{spec}}, x_{\text{spat}}) - F_{\text{sky}}(x_{\text{spec}}, x_{\text{spat}})]} \right]}. \quad (\text{A2})$$







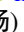





To model the sky background, which consists of both the sky emission and the host galaxy continuum, we also assume its linear dependence on wavelength,


$$F_{\text{sky}}(x_{\text{spec}}, x_{\text{spat}}) = k_{\text{sky}}x_{\text{spec}} + b_{\text{sky}}. \quad (\text{A3})$$

Outside the $H\alpha$ region, the sum of $F_{\text{SN,con}}$ and F_{sky} should be a good representation of the total flux. To find the optimized model parameters (k_{SN} , b_{SN} , k_{sky} , b_{sky}), we minimize the residual sum of squares outside the $H\alpha$ mask. The resultant models are presented in the middle panels of Figure 9.

The right panels of Figure 9 show the flux residuals, which should correspond to the narrow $H\alpha$ emission of both the host galaxy and the SN. In each panel, we overlay the FWHM of the SN trace as dotted lines. In the +1.3-day LT/SPRAT spectrum, there is a blob of emission features right at the center of the SN trace (see also Figure 7), whose centroid is ~ 1 pixel rightward of the centroid of the host emission. This indicates the existence of another $H\alpha$ component that is slightly ($\sim 10^2 \text{ km s}^{-1}$) redshifted relative to the galaxy background, which is consistent with a flash feature of the SN. In the NOT/ALFOSC spectrum obtained at nearly the same time, the emission emerges at the consistent wavelength. There is no evidence of such an offset component in the +2.3-day and +3.4-day spectra, confirming that the $H\alpha$ flash feature appears to be absent by +2.3 days. A narrow $H\alpha$ feature is visible in the +3.4-day 1D spectrum (Figure 7), but the location of this emission feature in the 2D spectrum is consistent with the centroid of the host emission. Thus, the $H\alpha$ feature in the 1D spectrum is contamination from the host and not a flash feature originating from the SN.

ORCID iDs

Nabeel Rehemtulla  <https://orcid.org/0000-0002-5683-2389>
W. V. Jacobson-Galán  <https://orcid.org/0000-0002-3934-2644>
Avinash Singh  <https://orcid.org/0000-0003-2091-622X>
Adam A. Miller  <https://orcid.org/0000-0001-9515-478X>
Charles D. Kilpatrick  <https://orcid.org/0000-0002-5740-7747>
K-Ryan Hinds  <https://orcid.org/0000-0002-0129-806X>
Chang Liu (刘畅)  <https://orcid.org/0000-0002-7866-4531>
Steve Schulze  <https://orcid.org/0000-0001-6797-1889>
Jesper Sollerman  <https://orcid.org/0000-0003-1546-6615>
Theophile Jegou du Laz  <https://orcid.org/0009-0003-6181-4526>
Tomás Ahumada  <https://orcid.org/0000-0002-2184-6430>
Katie Auchettl  <https://orcid.org/0000-0002-4449-9152>

S. J. Brennan  <https://orcid.org/0000-0003-1325-6235>
 Michael W. Coughlin  <https://orcid.org/0000-0002-8262-2924>
 Christoffer Fremling  <https://orcid.org/0000-0002-4223-103X>
 Anjasha Gangopadhyay  <https://orcid.org/0000-0002-3884-5637>
 Daniel A. Perley  <https://orcid.org/0000-0001-8472-1996>
 Nikolaus Z. Prusinski  <https://orcid.org/0000-0001-5847-7934>
 Josiah Purdum  <https://orcid.org/0000-0003-1227-3738>
 Yu-Jing Qin  <https://orcid.org/0000-0003-3658-6026>
 Sara Romagnoli  <https://orcid.org/0009-0003-8153-9576>
 Jennifer Shi  <https://orcid.org/0009-0008-3724-1824>
 Jacob L. Wise  <https://orcid.org/0000-0003-0733-2916>
 Tracy X. Chen  <https://orcid.org/0000-0001-9152-6224>
 Steven L. Groom  <https://orcid.org/0000-0001-5668-3507>
 David O. Jones  <https://orcid.org/0000-0002-6230-0151>
 Mansi M. Kasliwal  <https://orcid.org/0000-0002-5619-4938>
 Roger Smith  <https://orcid.org/0000-0001-7062-9726>
 Shrinivas R. Kulkarni  <https://orcid.org/0000-0001-5390-8563>

References

- Abadi, M., Agarwal, A., Barham, P., et al. 2015, arXiv:1603.04467
- Albareti, F. D., Allende Prieto, C., Almeida, A., et al. 2017, *ApJS*, **233**, 25
- Andrews, J. E., Pearson, J., Hosseinzadeh, G., et al. 2024, *ApJ*, **965**, 85
- Angus, C., Rojas-Bravo, C., DeMarchi, L., & Jacobson-Galan, W. 2021, *TNSCR*, **1**, 2021
- Astropy Collaboration, Price-Whelan, A. M., Lim, P. L., et al. 2022, *ApJ*, **935**, 167
- Astropy Collaboration, Price-Whelan, A. M., Sipőcz, B. M., et al. 2018, *AJ*, **156**, 123
- Astropy Collaboration, Robitaille, T. P., Tollerud, E. J., et al. 2013, *A&A*, **558**, A33
- Barbary, K. 2017, extinction v0.3.0, Zenodo, doi:10.5281/zenodo.804967
- Barnsley, R. M., Smith, R. J., & Steele, I. A. 2012, *AN*, **333**, 101
- Beasor, E. R., Davies, B., Smith, N., et al. 2020, *MNRAS*, **492**, 5994
- Becker, A. 2015 HOTPANTS: High Order Transform of PSF And Template Subtraction, Astrophysics Source Code Library, ascl:1504.004
- Behnel, S., Bradshaw, R., Citro, C., et al. 2011, *CSE*, **13**, 31
- Bellm, E. C., Kulkarni, S. R., Barlow, T., et al. 2019a, *PASP*, **131**, 068003
- Bellm, E. C., Kulkarni, S. R., Graham, M. J., et al. 2019b, *PASP*, **131**, 018002
- Berger, E., Keating, G. K., Margutti, R., et al. 2023, *ApJL*, **951**, L31
- Biewald, L., 2020 Experiment Tracking with Weights and Biases, <https://www.wandb.com/>
- Blagorodnova, N., Neill, J. D., Walters, R., et al. 2018, *PASP*, **130**, 035003
- Blinnikov, S., Lundqvist, P., Bartunov, O., Nomoto, K., & Iwamoto, K. 2000, *ApJ*, **532**, 1132
- Blinnikov, S. I., Eastman, R., Bartunov, O. S., Popolitov, V. A., & Woosley, S. E. 1998, *ApJ*, **496**, 454
- Blinnikov, S. I., Röpke, F. K., Sorokina, E. I., et al. 2006, *A&A*, **453**, 229
- Bloom, J. S., Richards, J. W., Nugent, P. E., et al. 2012, *PASP*, **124**, 1175
- Boian, I., & Groh, J. H. 2019, *A&A*, **621**, A109
- Boian, I., & Groh, J. H. 2020, *MNRAS*, **496**, 1325
- Boone, K. 2019, *AJ*, **158**, 257
- Bostroem, K. A., Pearson, J., Shrestha, M., et al. 2023, *ApJL*, **956**, L5
- Brink, H., Richards, J. W., Poznanski, D., et al. 2013, *MNRAS*, **435**, 1047
- Brown, T. M., Baliber, N., Bianco, F. B., et al. 2013, *PASP*, **125**, 1031
- Bruch, R. J., Gal-Yam, A., Schulze, S., et al. 2021, *ApJ*, **912**, 46
- Bruch, R. J., Gal-Yam, A., Yaron, O., et al. 2023, *ApJ*, **952**, 119
- Bullivant, C., Smith, N., Williams, G. G., et al. 2018, *MNRAS*, **476**, 1497
- Capaccioli, M., Della Valle, M., D'Onofrio, M., & Rosino, L. 1989, *AJ*, **97**, 1622
- Carr, A., Davis, T. M., Camilleri, R., et al. 2024, *PASA*, **41**, e068
- Carrasco-Davis, R., Reyes, E., Valenzuela, C., et al. 2021, *AJ*, **162**, 231
- Cenko, S. B., Fox, D. B., Moon, D.-S., et al. 2006, *PASP*, **118**, 1396
- Chambers, K. C., Magnier, E. A., Metcalfe, N., et al. 2016, arXiv:1612.05560
- Childress, M. J., Vogt, F. P. A., Nielsen, J., & Sharp, R. G. 2014, *Ap&SS*, **349**, 617
- Chollet, F., et al., 2015 Keras, <https://Keras.io>
- Chugai, N. N. 1991, *SvAL*, **17**, 210
- Chugai, N. N., & Urobin, V. P. 2023, *AstL*, **49**, 639
- Cook, D., Mazzarella, J., Helou, G., et al. 2025, *TNSAN*, **55**, 1
- Cook, D. O., Mazzarella, J. M., Helou, G., et al. 2023, *ApJS*, **268**, 14
- Coughlin, M. W., Bloom, J. S., Nir, G., et al. 2023, *ApJS*, **267**, 31
- da Costa-Luis, C. 2019, *JOSS*, **4**, 1277
- Davis, K. W., Taggart, K., Tinyanont, S., et al. 2023, *MNRAS*, **523**, 2530
- De, K., Kasliwal, M. M., Tzanidakis, A., et al. 2020, *ApJ*, **905**, 58
- de Vaucouleurs, G., de Vaucouleurs, A., Corwin Herold, G. J., et al. 1991, Third Reference Catalogue of Bright Galaxies (New York: Springer)
- Dekany, R., Smith, R. M., Riddle, R., et al. 2020, *PASP*, **132**, 038001
- D'Elia, V., Fiore, F., Perna, R., et al. 2009, *ApJ*, **694**, 332
- Dessart, L., Hillier, D. J., & Audit, E. 2017, *A&A*, **605**, A83
- Dessart, L., & Jacobson-Galán, W. V. 2023, *A&A*, **677**, A105
- Dickinson, D., Milisavljevic, D., Garretson, B., et al. 2025, *ApJ*, **984**, 71
- Dopita, M., Hart, J., McGregor, P., et al. 2007, *Ap&SS*, **310**, 255
- Dopita, M., Rhee, J., Farage, C., et al. 2010, *Ap&SS*, **327**, 245
- Duev, D., Shin, K. M., & Singer, L. 2021, dmitryduev/penquins: A Python Client for dmitryduev/kowalski, v2.1.2, Zenodo, doi:10.5281/zenodo.5651471
- Duev, D. A., Mahabal, A., Masci, F. J., et al. 2019, *MNRAS*, **489**, 3582
- Duev, D. A., & van der Walt, S. J. 2021, arXiv:2111.12142
- Fabricant, D., Fata, R., Epps, H., et al. 2019, *PASP*, **131**, 075004
- Fazio, G. G., Hora, J. L., Allen, L. E., et al. 2004, *ApJS*, **154**, 10
- Fitzpatrick, E. L. 1999, *PASP*, **111**, 63
- Fremling, C., Hall, X. J., Coughlin, M. W., et al. 2021, *ApJL*, **917**, L2
- Fremling, C., Miller, A. A., Sharma, Y., et al. 2020, *ApJ*, **895**, 32
- Fremling, C., Sollerman, J., Taddia, F., et al. 2016, *A&A*, **593**, A68
- Gagliano, A., Contardo, G., Foreman-Mackey, D., Malz, A. I., & Aleo, P. D. 2023, *ApJ*, **954**, 6
- Gal-Yam, A., Arcavi, I., Ofek, E. O., et al. 2014, *Natur*, **509**, 471
- Gangopadhyay, A., Misra, K., Hiramatsu, D., et al. 2020, *ApJ*, **889**, 170
- Gangopadhyay, A., Misra, K., Hosseinzadeh, G., et al. 2022, *ApJ*, **930**, 127
- Gehrels, N., Chincarini, G., Giommi, P., et al. 2004, *ApJ*, **611**, 1005
- Ginsburg, A., Sipőcz, B., Brasseur, C. E., et al. 2024, astropy/astroquery: v0.4.7, Zenodo, doi:10.5281/zenodo.10799414
- Ginsburg, A., Sipőcz, B. M., Brasseur, C. E., et al. 2019, *AJ*, **157**, 98
- Goldberg, J. A., Bildsten, L., & Paxton, B. 2019, *ApJ*, **879**, 3
- Gomez, S., Berger, E., Blanchard, P. K., et al. 2020, *ApJ*, **904**, 74
- Gomez, S., Villar, V. A., Berger, E., et al. 2023, *ApJ*, **949**, 113
- Gommers, R., Virtanen, P., Haberland, M., et al. 2024, scipy/scipy: SciPy v1.14.1, Zenodo, doi:10.5281/zenodo.13352243
- González, M., Audit, E., & Huynh, P. 2007, *A&A*, **464**, 429
- Graham, M. J., Kulkarni, S. R., Bellm, E. C., et al. 2019, *PASP*, **131**, 078001
- Green, G. 2018, *JOSS*, **3**, 695
- Green, G., Edenhofer, G., Krughoff, S., et al. 2024, gregreen/dustmaps: v1.0.13, Zenodo, doi:10.5281/zenodo.10517733
- Hamuy, M. 2003, *ApJ*, **582**, 905
- Harris, C. R., Millman, K. J., van der Walt, S. J., et al. 2020, *Natur*, **585**, 357
- Hillier, D. J., & Dessart, L. 2012, *MNRAS*, **424**, 252
- Hinds, K.-R., Perley, D., & Sollerman, J. 2025, arXiv:2503.19969
- Hinds, K., Sollerman, J., Fremling, C., Perley, D., & Laz, T. D. 2024, *TNSTR*, **1**, 2024
- Hiramatsu, D., Arcavi, I., Zimmerman, E., et al. 2020, *TNSCR*, **1**, 2020
- Hiramatsu, D., Tsuna, D., Berger, E., et al. 2023, *ApJL*, **955**, L8
- Hosseinzadeh, G., Howell, D. A., McCully, C., et al. 2024, *TNSCR*, 2024-1686, 1
- Howell, D. A. & Global Supernova Project 2017, AAS Meeting Abstracts, **230**, 318.03
- Hunter, J. D. 2007, *CSE*, **9**, 90
- Irani, I., Morag, J., Gal-Yam, A., et al. 2024, *ApJ*, **970**, 96
- Izzo, L., Angus, C., Hjorth, J., & Gall, C. 2020, *TNSCR*, **1**, 2020
- Jacobson-Galán, W. V., Davis, K. W., Kilpatrick, C. D., et al. 2024a, *ApJ*, **972**, 177
- Jacobson-Galán, W. V., Dessart, L., Davis, K. W., et al. 2024b, *ApJ*, **970**, 189
- Jacobson-Galán, W. V., Dessart, L., Jones, D. O., et al. 2022, *ApJ*, **924**, 15
- Jacobson-Galán, W. V., Dessart, L., Margutti, R., et al. 2023, *ApJL*, **954**, L42
- Jones, D. O., Foley, R. J., Narayan, G., et al. 2021, *ApJ*, **908**, 143
- Kaiser, N., Aussel, H., Burke, B. E., et al. 2002, *Proc. SPIE*, **4836**, 154
- Khazov, D., Yaron, O., Gal-Yam, A., et al. 2016, *ApJ*, **818**, 3
- Kilpatrick, C. D., & Foley, R. J. 2018, *MNRAS*, **481**, 2536
- Kim, Y. L., Rigault, M., Neill, J. D., et al. 2022, *PASP*, **134**, 024505
- Kluyver, T., Ragan-Kelley, B., Pérez, F., et al. 2016, Positioning and Power in Academic Publishing: Players, Agents and Agendas (Amsterdam: IOS Press), 87
- Martin, C., Moore, A., Morrissey, P., et al. 2010, *Proc. SPIE*, **7735**, 77350M
- Masci, F. J., Laher, R. R., Rusholme, B., et al. 2019, *PASP*, **131**, 018003
- Masci, F. J., Laher, R. R., Rusholme, B., et al. 2023, arXiv:2305.16279
- Matheson, T., Filippenko, A. V., Barth, A. J., et al. 2000, *AJ*, **120**, 1487
- McKinney, W. 2010, in Proc. 9th Python in Science Conf., ed. S. van der Walt & J. Millman (Austin, TX: SciPy), 56
- Miller, A. A., Yao, Y., Bulla, M., et al. 2020, *ApJ*, **902**, 47

- Miranda, N., Freytag, J. C., Nordin, J., et al. 2022, *A&A*, **665**, A99
- Moriya, T. J., & Singh, A. 2024, *PASJ*, **76**, 1050
- Moriya, T. J., Subrayan, B. M., Milisavljevic, D., & Blinnikov, S. I. 2023, *PASJ*, **75**, 634
- Morrissey, P., Matuszewski, M., Martin, D. C., et al. 2018, *ApJ*, **864**, 93
- Muthukrishna, D., Narayan, G., Mandel, K. S., Biswas, R., & Hložek, R. 2019, *PASP*, **131**, 118002
- Nasa High Energy Astrophysics Science Archive Research Center (Heasarc), 2014 HEASoft: Unified Release of FTOOLS and XANADU, Astrophysics Source Code Library, ascl:1408.004
- NASA/IPAC Extragalactic Database (NED) 2019, NASA/IPAC Extragalactic Database (NED)
- Niemela, V. S., Ruiz, M. T., & Phillips, M. M. 1985, *ApJ*, **289**, 52
- Nordin, J., Brinnel, V., van Santen, J., et al. 2019, *A&A*, **631**, A147
- Oke, J. B., Cohen, J. G., Carr, M., et al. 1995, *PASP*, **107**, 375
- Pastorello, A., Sauer, D., Taubenberger, S., et al. 2006, *MNRAS*, **370**, 1752
- Pearson, J., Hosseinzadeh, G., Sand, D. J., et al. 2023, *ApJ*, **945**, 107
- Pejcha, O., & Prieto, J. L. 2015, *ApJ*, **806**, 225
- Perez, F., & Granger, B. E. 2007, *CSE*, **9**, 21
- Perley, D. A., Fremling, C., Sollerman, J., et al. 2020, *ApJ*, **904**, 35
- Perley, D. A., Sollerman, J., Schulze, S., et al. 2022, *ApJ*, **927**, 180
- Phillips, M. M., Simon, J. D., Morrell, N., et al. 2013, *ApJ*, **779**, 38
- Piascik, A. S., Steele, I. A., Bates, S. D., et al. 2014, *Proc. SPIE*, **9147**, 91478H
- Poznanski, D., Ganeshalingam, M., Silverman, J. M., & Filippenko, A. V. 2011, *MNRAS*, **415**, L81
- Prochaska, J. X., Hennawi, J. F., Westfall, K. B., et al. 2020, *JOSS*, **5**, 2308
- Rehemtulla, N., Fremling, C., Perley, D., & Laz, T. D. 2025, *TNSTR*, **1**, 2025
- Rehemtulla, N., Laz, T. J. D., Schulze, S., et al. 2024a, *TNSAN*, **140**, 1
- Rehemtulla, N., Miller, A., Fremling, C., et al. 2023, *TNSAN*, **265**, 1
- Rehemtulla, N., Miller, A. A., Jegou Du Laz, T., et al. 2024b, *ApJ*, **972**, 7
- Rest, A., Stubbs, C., Becker, A. C., et al. 2005, *ApJ*, **634**, 1103
- Rigault, M., Neill, J. D., Blagorodnova, N., et al. 2019, *A&A*, **627**, A115
- Roming, P. W. A., Kennedy, T. E., Mason, K. O., et al. 2005, *SSRv*, **120**, 95
- Schechter, P. L., Mateo, M., & Saha, A. 1993, *PASP*, **105**, 1342
- Schlafly, E. F., & Finkbeiner, D. P. 2011, *ApJ*, **737**, 103
- Schulze, S., Gal-Yam, A., Dessart, L., et al. 2024, arXiv:2409.02054
- Schulze, S., Yaron, O., Sollerman, J., et al. 2021, *ApJS*, **255**, 29
- Sharma, Y., Mahabal, A. A., Sollerman, J., et al. 2025, *PASP*, **137**, 034507
- Shivvers, I., Groh, J. H., Mauerhan, J. C., et al. 2015, *ApJ*, **806**, 213
- Shrestha, M., Bostroem, K. A., Sand, D. J., et al. 2024, *ApJL*, **972**, L15
- Singh, A., Kumar, B., Moriya, T. J., et al. 2019, *ApJ*, **882**, 68
- Singh, A., Teja, R. S., Moriya, T. J., et al. 2024, *ApJ*, **975**, 132
- Smith, K. W., Smartt, S. J., Young, D. R., et al. 2020, *PASP*, **132**, 085002
- Sollerman, J., Yang, S., Schulze, S., et al. 2021, *A&A*, **655**, A105
- Sorce, J. G., Tully, R. B., Courtois, H. M., et al. 2014, *MNRAS*, **444**, 527
- Soumagnac, M. T., Ganot, N., Irani, I., et al. 2020, *ApJ*, **902**, 6
- Steele, I. A., Smith, R. J., Rees, P. C., et al. 2004, *Proc. SPIE*, **5489**, 679
- Stein, R., Mahabal, A., Reusch, S., et al. 2024, *ApJL*, **965**, L14
- Street, R. A., Adamson, A., Blakeslee, J. P., et al. 2020, *Proc. SPIE*, **11449**, 1144925
- Stritzinger, M. D., Taddia, F., Burns, C. R., et al. 2018, *A&A*, **609**, A135
- Sukhbold, T., Ertl, T., Woosley, S. E., Brown, J. M., & Janka, H. T. 2016, *ApJ*, **821**, 38
- Szalai, T., Vinkó, J., Könyves-Tóth, R., et al. 2019, *ApJ*, **876**, 19
- Taggart, K., Tinyanont, S., Foley, R. J., & Gagliano, A. 2021, *ATel*, **14959**, 1
- Tartaglia, L., Sand, D. J., Groh, J. H., et al. 2021, *ApJ*, **907**, 52
- Tartaglia, L., Sand, D. J., Valenti, S., et al. 2018, *ApJ*, **853**, 62
- Teja, R. S., Singh, A., Basu, J., et al. 2023, *ApJL*, **954**, L12
- Terreran, G., Jacobson-Galan, W., & Blanchard, P. K. 2020, *ATel*, **14115**, 1
- Terreran, G., Jacobson-Galán, W. V., Groh, J. H., et al. 2022, *ApJ*, **926**, 20
- The pandas development team 2024, pandas-dev/pandas: Pandas, v2.2.3, Zenodo, doi:10.5281/zenodo.13819579
- Tohuvavohu, A., Kennea, J. A., Roberts, C. J., et al. 2024, *ApJL*, **975**, L19
- Tonry, J. L. 2011, *PASP*, **123**, 58
- Tonry, J. L., Denneau, L., Heinze, A. N., et al. 2018, *PASP*, **130**, 064505
- Tully, R. B., & Fisher, J. R. 1977, *A&A*, **54**, 661
- van der Walt, S. J., Crellin-Quick, A., & Bloom, J. S. 2019, *JOSS*, **4**, 1247
- Van Rossum, G., & Drake, F. L. 2009, *Python 3 Reference Manual* (Scotts Valley, CA: CreateSpace)
- Villar, V. A., Berger, E., Miller, G., et al. 2019, *ApJ*, **884**, 83
- Villar, V. A., Hosseinzadeh, G., Berger, E., et al. 2020, *ApJ*, **905**, 94
- Virtanen, P., Gommers, R., Oliphant, T. E., et al. 2020, *NatMe*, **17**, 261
- Wagg, T., Broekgaarden, F., & Gültekin, K. 2024, TomWagg/software-citation-station: v1.2
- Wagg, T., & Broekgaarden, F. S. 2024, arXiv:2406.04405
- Yang, S., Sollerman, J., Strotjohann, N. L., et al. 2021, *A&A*, **655**, A90
- Yaron, O., Perley, D. A., Gal-Yam, A., et al. 2017, *NatPh*, **13**, 510
- York, D. G., Adelman, J., Anderson John, E. J., et al. 2000, *AJ*, **120**, 1579
- Zhang, J., Wang, X., József, V., et al. 2020, *MNRAS*, **498**, 84
- Zimmerman, E. A., Irani, I., Chen, P., et al. 2024, *Natur*, **627**, 759